

**ALMA MATER STUDIORUM - UNIVERSITÀ DI  
BOLOGNA**

---

**SCUOLA DI INGEGNERIA E ARCHITETTURA**

*DIPARTIMENTO DI INGEGNERIA CHIMICA, AMBIENTALE E DEI  
MATERIALI*

*Corso di Laurea in Civil Engineering*

**TESI DI LAUREA**

in  
Advanced Design of Structures

**DYNAMIC CHARACTERISATION OF FOUR NINE-STORY  
LARGE-PANEL R.C. BUILDINGS IN BISHKEK  
(KYRGYZSTAN): A COMPARISON BETWEEN  
EXPERIMENTAL AMBIENT VIBRATION ANALYSIS AND  
NUMERICAL FINITE ELEMENT MODELING**

Candidato:  
ELISA MASSARI

Relatore:  
Chiar.mo Prof. Ing. Stefano Silvestri

Correlatori:  
Prof. Dr. Stefano Parolai  
Dipl. –Phys. Bojana Petrovic

Anno Accademico 2014/2015

Sessione III



# Contents

<b>1</b>	<b>Introduction</b>	<b>4</b>
1.1	Background . . . . .	4
1.2	Objectives of the research . . . . .	8
1.3	Organization of the text . . . . .	9
<b>2</b>	<b>Case studies</b>	<b>10</b>
2.1	Description of the buildings . . . . .	10
2.2	Documentation . . . . .	12
2.3	Building inspections . . . . .	15
<b>3</b>	<b>Experimental ambient vibration analysis</b>	<b>21</b>
3.1	Measurement set-up and data pre-processing . . . . .	21
3.2	Spectral analysis . . . . .	25
3.2.1	Methodology . . . . .	25
3.2.2	Analysis . . . . .	27
3.2.3	Results . . . . .	28
3.3	Modal analysis with the Frequency Domain Decomposition . .	32
3.3.1	Methodology . . . . .	32
3.3.2	Analysis . . . . .	34
3.3.3	Results . . . . .	34

3.4	Interferometric analysis . . . . .	43
3.4.1	Methodology . . . . .	43
3.4.2	Analysis . . . . .	46
3.4.3	Results . . . . .	47
<b>4</b>	<b>Numerical Finite Element modelling</b>	<b>58</b>
4.1	Methodology . . . . .	58
4.1.1	Modal Analysis . . . . .	58
4.2	Analysis . . . . .	61
4.2.1	Geometry and mesh size . . . . .	63
4.2.2	Materials . . . . .	64
4.2.3	Loads and masses . . . . .	65
4.3	Results . . . . .	67
<b>5</b>	<b>Comparison between experimental and numerical results</b>	<b>70</b>
<b>6</b>	<b>Calibration of the numerical models</b>	<b>74</b>
6.1	Methodologies . . . . .	75
6.1.1	Elastic Keys . . . . .	75
6.1.2	Distribution of the internal walls . . . . .	75
6.1.3	Material properties . . . . .	76
6.1.4	Seismic joint . . . . .	77
6.2	Analysis . . . . .	77
6.3	Results of the calibration . . . . .	79
<b>7</b>	<b>Conclusions</b>	<b>83</b>
7.1	Analysis conducted . . . . .	83
7.2	Results obtained . . . . .	84
7.3	Future developments . . . . .	85

<b>8</b>	<b>References</b>	<b>86</b>
<b>9</b>	<b>Appendix 1: Photos of the buildings</b>	<b>90</b>
<b>10</b>	<b>Appendix 2: FFT spectra</b>	<b>102</b>

# Chapter 1

## Introduction

### 1.1 Background

Central Asia is a region with high seismic hazard, resulting from the collision between the Indian and Eurasian plates (Molnar and Tapponnier, 1975, 1978), which takes place in the Hindu Kush and Himalaya region. Seismic hazard is a probabilistic concept, which defines the probability of a given level of ground motion to occur in a given area and time window. The evaluation of seismic hazard as a prediction and design tool is mainly based on records of past seismic events in the region of interest. Records of large earthquakes in Central Asia are available for the last two centuries (World Data Center, 1982); they include events of significant magnitude in the northern part of the Tien Shan mountain range (M=8,2 1889 Chilik earthquake; M=8,2 1911 Kemin earthquake; M=6,9 1938 Chu-Kemin earthquake). Probabilistic seismic hazard assessment (PSHA) for Central Asia has therefore been the goal of many studies at different spacial scales (Ulomov, 1999; Bindi *et al.*, 2012; Ullah *et al.*, 2015).

Seismic hazard is one of the three probabilistic components that define seis-

mic risk. The other two are seismic vulnerability, which estimates the damage to structures and infrastructures resulting from a certain level of ground motion in the area, and exposure, which considers essentially the assets exposed to damage in the area. Seismic risk is the result of these three variables and can be defined as the probability of an entity to be damaged as consequence of a seismic event of a certain magnitude in a given area. Seismic risk can be defined from economic, social or environmental points of view, according to what is considered as being exposed population.

In order to reduce seismic risk, the main focus of intervention is vulnerability. In seismic regions, reducing the structural vulnerability is prescribed as a goal of the structural design. Unfortunately reality shows that this kind of prescription is sometimes neglected during the construction phase. This seems to be the case also for a number of existing buildings in Central Asia, where the effects of past earthquakes suggest that the vulnerability of the buildings is actually higher than expected (Nurmagambetov, 1999; GeoHazard International, 1997). Because of the centralization of design and construction practices in the former U.S.S.R., similar structural systems can be found throughout the region. GeoHazard International (1997) has identified six structural types, out of which only precast RC large-panel systems are said to present a fairly low seismic vulnerability.

The city of Bishkek (see Figure 1.1), the capital of Kyrgyzstan, has experienced during the last fifty years a steep increase in its population, together with the expansion of the urban area. This relatively new scenario in terms of seismic risk has established Bishkek as a significant case study in Central Asia. Considering the geomorphological setting, Bishkek is located in the Chu basin, one of the largest depressions of the Tien Shan mountain region. The Issyk-Ata fault system, in the Kyrgyz Range, controls the seismic hazard

of Bishkek and is located on the southern bounds of the Chu basin. Looking at the geology of the area, the depth of the Paleozoic basement ranges from 1 km (northern part of the city) to 3 km (southern part of the city). Quaternary sediments of the Ala-Archa and Alamedin rivers form the uppermost layer, with a thickness of 200-300 m. Parolai *et al.* (2010) showed that, although these alluvial materials are quite stiff, they are responsible for significant site amplification effects over a broad frequency range. This means that the amplitude of ground motion will be larger for several frequency components, as a result of the dynamic properties of the upper sediments. This effect generally increases the stress on the structures and can also lead to failure of the foundation system. Bindi *et al.* (2011) developed a deterministic risk scenario for Bishkek, taking site amplification into account, and showed that a magnitude 7,5 earthquake at the Issyk-Ata fault would cause the collapse of 21 794 buildings and 21 794 fatalities over 77 148 existing buildings and a population of 849 204. In this work the vulnerability was estimated according to the classification of the European Macroseismic Scale 1998, EMS-98 (Grünthal, 1998), considering the percentage of buildings belonging to each vulnerability class as a homogeneous value throughout the city area. It was pointed out (Bindi *et al.*, 2011) that a vulnerability model at the district scale should be a further step in the hazard assessment. In the framework of the Earthquake Model Central Asia<sup>1</sup> (EMCA) project, Wieland *et al.* (2012) proposed an integrated approach to estimating the building inventory for seismic vulnerability assessment, using satellite remote sensing and ground-based omnidirectional imaging to map building typologies over a given area. This method optimizes the amount of information required with a top-down analysis, acquiring more detailed information only if they are

---

<sup>1</sup><http://www.emca-gem.org/>



necessary. Knowing the building typology distribution, the vulnerability can be assigned on a district scale, according to the classification of the present buildings. In addition, ambient vibration analysis has been used to characterise the dynamic behaviour of five building typologies in Bishkek (Petryna *et al.*, 2014; Petrovic *et al.*, 2014). For this purpose, Petryna *et al.* (2014) retrieved the modal characteristics and the average shear wave velocity in the structure for five different buildings. Continuing the approach followed by Petrovic *et al.* (2014) and Petryna *et al.* (2014), this work improves the evaluation of the level of damage that can occur, if such structural systems are subjected to dynamic shaking.

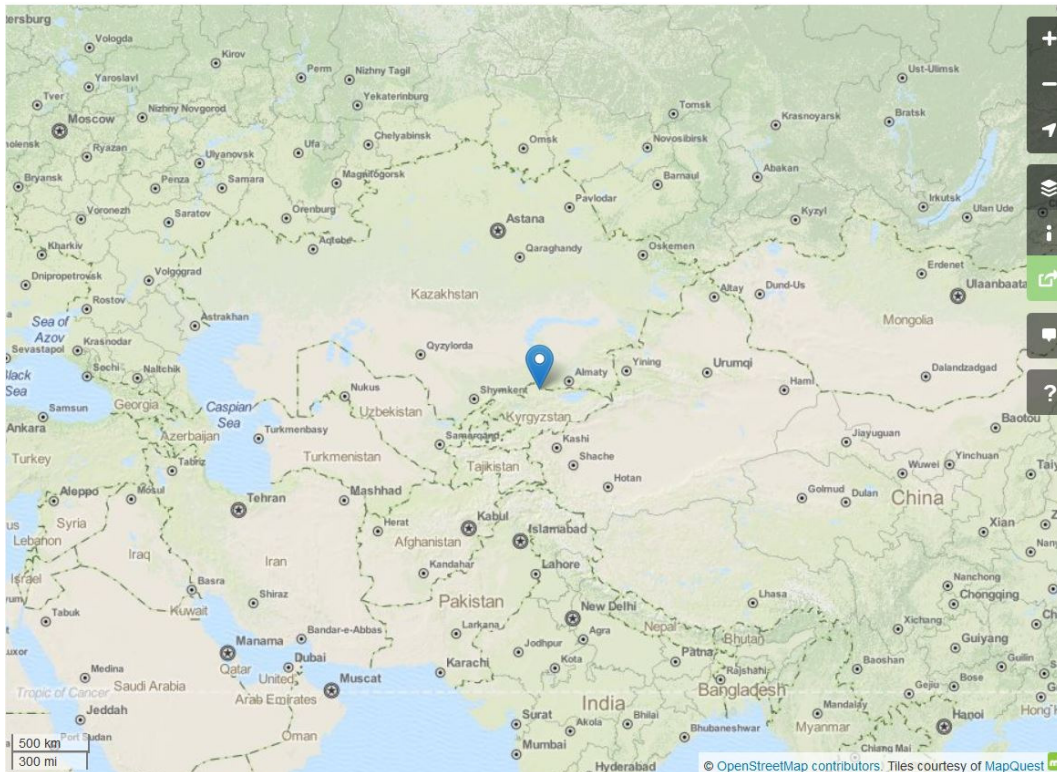


Figure 1.1: Location of Bishkek, capital city of Kyrgyzstan. (Source: OpenStreetMap)

## 1.2 Objectives of the research

This thesis contributes to our capacity for the dynamic characterisation of precast reinforced concrete (r.c.) large-panel buildings in Bishkek, with the outlook of improving vulnerability models for this structural type.

To this purpose, ambient vibrations measurements were performed in four r. c. large-panel buildings. In this way, we recorded the structural response to the dynamic excitation of the so-called ambient noise, which is the combination of all vibrations produced by natural or anthropogenic sources that can be recorded in the area. This dynamic input usually includes a fairly wide frequency range, which allows one to identify those frequencies that are natural frequencies of the buildings. Furthermore, ambient noise provides a dynamic input of very small amplitude, which guarantees that the structural behaviour is linear elastic.

A first objective is therefore to obtain experimentally the values of some parameters that characterize the structures' dynamic behaviour (fundamental frequency, first modes of vibration, wave propagation velocity in elastic regime). These buildings all belong to the series 105: this means that they were all built using r. c. panels with the same geometry and material characteristic. Small variations in plan or in the balcony distribution characterise each of the four buildings, which are otherwise very similar in design.

A second goal of this work is to see if it is possible to set up a numerical Finite Element model that describes the global dynamic behaviour of different buildings of the same typology. This information will contribute to the later improvement of a vulnerability model for the city of Bishkek.

The numerical modelling is based on the available information about geometry and materials of the buildings, which was in some aspects incomplete. A third objective of the thesis is to compare the experimental results with those

obtained numerically, based on partially incomplete information. Assuming that the experimental results computed from ambient vibration measurements are correct, a final goal is the calibration of the numerical model to the experimental results, looking at the global dynamic characteristics of the buildings.

### **1.3 Organization of the text**

After this Introduction, the case studies are presented (Chapter 2). The second chapter includes a description of the buildings, together with the report of the sources used to collect the information used in this work.

Chapter 3 presents the experimental analysis of the ambient vibration data. It starts with the description of the measurements set-up and is then divided into three parts: first, the spectral analysis is presented (Section 3.2); then the operational modal analysis (Section 3.3) and the interferometric analysis (Section 3.4) are reported. Chapter 4 focuses on the numerical model. It is also subdivided into three parts, dealing with the analysis methods (Section 4.1), the analysis setting (Section 4.2) and the results (Section 4.3).

Then, in Chapter 5, the experimental and numerical results are compared. This is the basis for the calibration of the model, in order to match the experimental results, presented in Chapter 6. Finally, Chapter 7 summarizes the results obtained with suggestions for future work.

# Chapter 2

## Case studies

### 2.1 Description of the buildings

The focus of this study are four large-panel (LP) buildings located in Bishkek. Two are symmetric in plan (number 37 and 43) and two asymmetric (number 25 and 4/1); all belong to the building series 105. Figure 2.1 shows the buildings' location on an OpenStreetMap web image. Their construction times varies between the 1960s and the 1980s. All structures were designed and have always been used for residential purpose. They all share the same construction technique and are very similar in plan. Their dimensions in plan are 39,6 m x 10,8 m and 40,5 m x 10,8 m for the symmetric and asymmetric in plan buildings, respectively. All buildings have nine three-meter high floors and a basement rising up to 0,9 m above the ground level, for a total height of 27,9 m. A distinction has to be made between building 43 and the other three: this stands, in fact, separated from other adjacent buildings. The other three, instead, are separated by a seismic joint from the neighbouring building with the same structure as the one studied.

In LP buildings, the load-bearing structure is composed of precast reinforced

concrete panels that are usually produced in standard sizes to fulfil the various purposes of construction (slab, internal or external walls, with or without openings) and assembled on the building site with partially cast in place joints. The construction process was done in series: the geometry of the structures has very little variation within the same series, because the same types of panels were used. In our case, the building series 105 features elements of only two standard dimensions: 3,60 m x 3,00 m for the larger panels ( $L$ ) and 2,70 m x 3,00 m for the smaller panels ( $S$ ). According to the distribution of these elements on the longitudinal dimension, the symmetric in plan buildings have the scheme  $LSLLSL LSLLSL$ , while the asymmetric in plan buildings have the scheme  $LSLLSL LSLLLL$ . The plans of the buildings are represented in Figures 2.2-2.4 .

Information about the buildings characteristics were collected through documentation and site inspection.

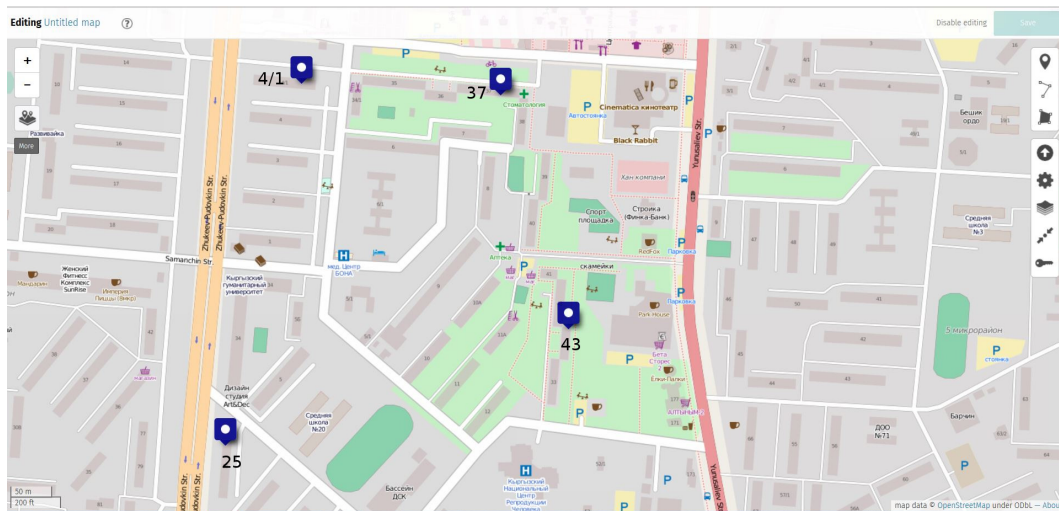


Figure 2.1: Location of the four buildings in Bishkek (Kyrgyzstan) (Source: OpenStreetMap).

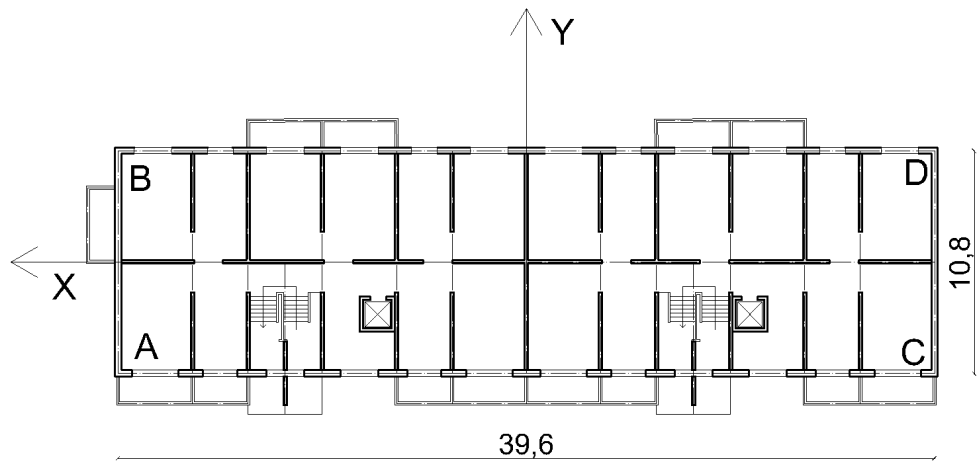


Figure 2.2: Plan view of building number 37. The plan is symmetric. On the right side an adjacent block is present (not shown in this figure), separated by a seismic joint. On the plan, the locations of the seismic recorders (A, B, C, D) are presented, together with a conventional cartesian system.

## 2.2 Documentation

The buildings' characteristics have been reconstructed on the basis of two main sources: the information about the series 105 buildings that is available from the World Housing Encyclopedia (WHE) and a plan view referred to this series archived at the Kyrgyz State University of Construction, Transport and Architecture (<http://www.ksucta.kg/en/>) in Bishkek.

From the website of WHE (<http://db.world-housing.net/building/38>), a wide range of information is available. First, the geometry of the panels is given:

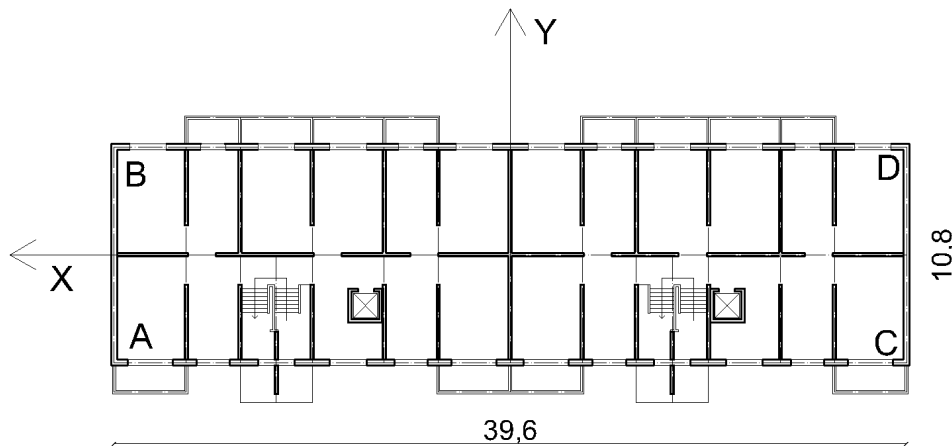


Figure 2.3: Plan view of the building number 43. The plan is symmetric. The buildings stands separated from adjacent structures. On the plan, the locations of the seismic recorders (A, B, C, D) are presented, together with a conventional cartesian system.

a summary of the dimensions of the different typologies is reported in Table 2.1. Then, the design and construction processes are documented. This includes information about the assembling of the panels. As Figure 2.5 shows, each precast element has vertical and horizontal steel dowels, which are to be joined together on the building site. Once the panels are placed in their final position, the dowels are welded and cast in place concrete is used to fill the gap between the panels. The final joint system is shown in Figure 2.6. It can be seen that the joints usually connect four panels. Another

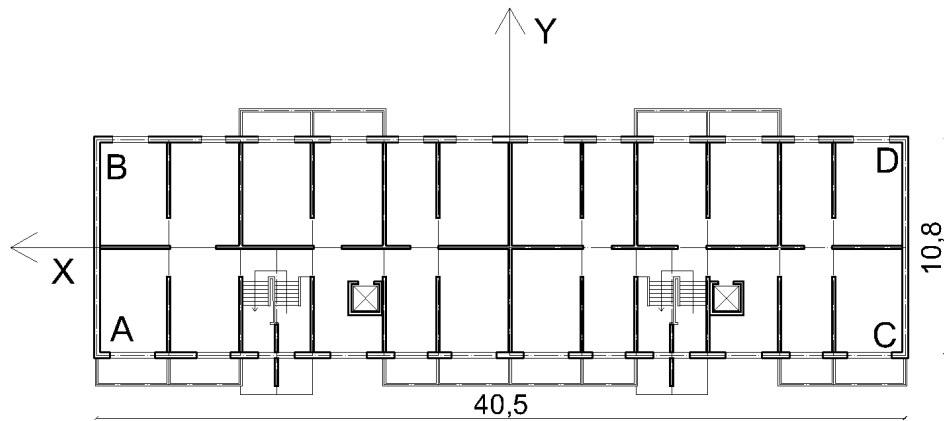


Figure 2.4: Plan view of the asymmetric buildings, number 25 and 4/1. The plan is asymmetric. Adjacent to this block, stands another block (not shown in this figure), separated by a seismic joint. On the plan, the locations of the seismic recorders (A, B, C, D) are presented, together with a conventional cartesian system.

important aspect documented on the WHE are the building materials. It is stated that vertical walls and slab panels are made of concrete with characteristic cube compressive strength between 20 and 30 MPa and that external walls are made of lightweight concrete. The WHE also provides information about the construction process. These buildings were designed taking seismic prescriptions into account, probably following the SNiP II-7-81 code or its previous version from 1962. It is noted that panel joints may be a shortcoming in the earthquake resistance of the structure. In fact, the quality of



the connections is considered to be poor in some cases, because of the inappropriate density of the concrete, missing alignment of the steel dowels and poor quality of welding. In general, these flaws are too few to compromise the overall resistance of the buildings. Cracking of joints (see Figure 2.8 for an example) could however be spotted in the buildings. With reference to the EMS98 (Grünthal, 1998), the buildings are considered to belong to vulnerability class E, between medium and low vulnerability. The second reference available is a plan view of a typical building from the series 105 (Figure 2.7). The plan does not show the whole length of the building, which is assumed to be symmetrical. This blueprint confirms the dimensions given by WHE and shows the position of the elevator and the stairs. The distribution of internal walls is also reported, although it was seen during the measurements that some of them have been torn down or moved by the tenants.

Table 2.1: Geometry data from WHE. The dimension of the precast structural elements are given.

Dimensions of large panels	360x300 cm
Dimensions of small panels	270x300 cm
Thickness of internal wall panels	16 cm
Thickness of external wall panels	30 cm
Window opening in large panels	182x153 cm
Window opening in small panels	124x153 cm
Balcony door in large panels	255x190 cm
Balcony door in small panels	166x190 cm

## 2.3 Building inspections

The inspection played a fundamental role in the buildings' characterization. The survey took place at two different times: firstly, the dimensions of the panels were roughly measured and their position documented. Then, after

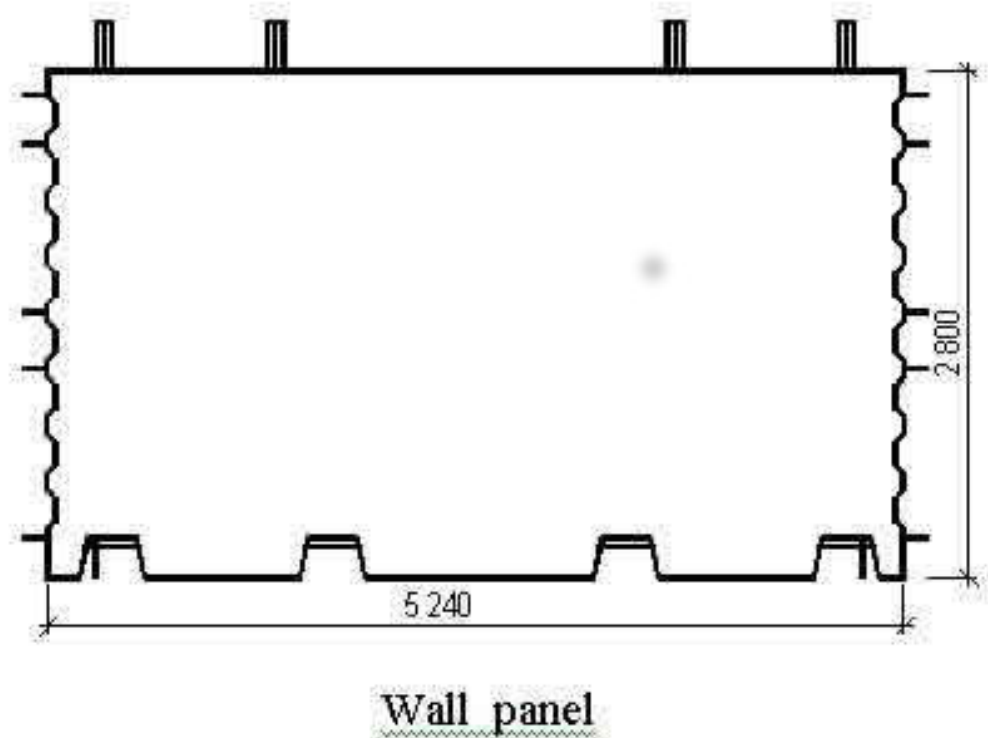


Figure 2.5: Structural detail of a wall panel (source WHE).

having read the available documentation (see Section 2.2), a second inspection was carried out, in order to check and integrate the information and to look for signs of damage on the structure. From the first inspection, it was clear that the panels had two different sizes, 3,6 m x 3,0 m (large panels) and 2,7 m x 3,0 m (small panels). The schemes used to combine these elements were also identified and the balcony distribution was documented. It was then possible to sketch the plan view of the buildings based on this information. In the second inspection, attention was paid to the basements, which have a variable height in the each building from 1 to 1,8 m, and are used as cellars and technical compartments. The positions of the internal walls in the basements do not vary with respect to the upper floors, but the panels have wide openings, in order to let pipes run along the building. It

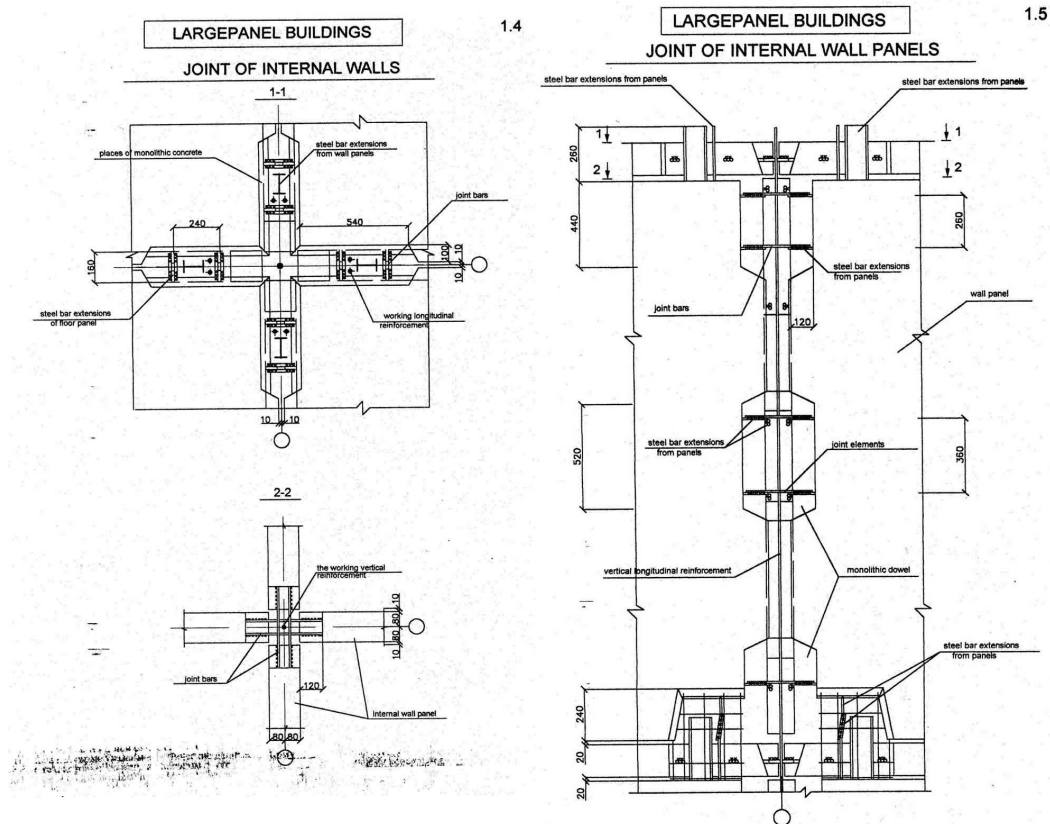


Figure 2.6: Structural detail of the joint for external wall panels - horizontal section on the left and vertical section on the right (Source: WHE).

was also possible to see an element of the foundation, which confirms that the buildings lie on a r. c. shallow mat foundation with strip footing.

The state of the joints between panels was documented: some of them show a vertical crack or a cracking pattern related to thermal stress, others are missing the cement cover. However, most joints have a proper concrete cover: it is implied then that the missing covers are construction flaws. These flaws are limited to a very few spots and even if they could cause a failure of the joint, this would probably be a local phenomenon. Connections with the balconies are often in a very poor condition: the connection between vertical and horizontal panels is often lacking the concrete cover on the outside. All

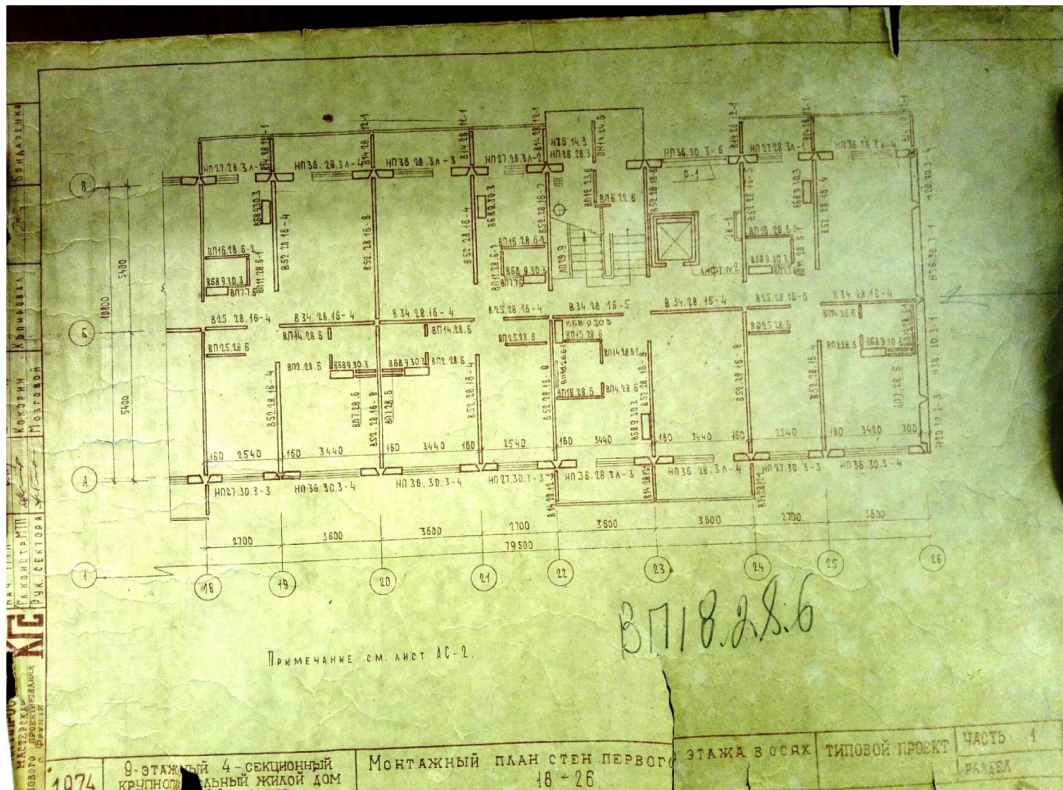


Figure 2.7: Plan view of a typical building of the series 105 (from the Institute of seismic-resistant construction in Bishkek). This plan shows only half of the building. We assumed that the other half would be symmetric, as could be observed from the building inspections for buildings 37 and 43. The distribution of the internal walls observed in the inspection is well represented in this plan.

these flaws were not considered in the numerical modelling, because they probably affect only the local behaviour.

It was observed that no joint is present between the slab and the balcony, which have then to be considered as one continuous panel. The vertical elements of the balconies also look like panel elements, which are connected together and to the external walls with the typical joint system. The balconies are often used as an internal part of the flat, as they are closed in by windows. In some rare cases, they are open.



Figure 2.8: Cracking of the joint reported in building 4/1, documented during the second inspection. The shape of the crack led us to believe that this could become a local point of failure in case of large ground motion excitation.

A further goal of the second survey was to see if the elevator and the stairs can be considered as non-structural parts or if they are integrated into the structure, in order to decide whether to include them in the numerical model. It was observed in the stairwell of all four buildings, that one of the two flight

of stairs between two floors is detached from all walls. The landing is also not connected to the external walls in a standard way, because the presence of a window in all buildings let the connection between landing and vertical walls be only at the two extremities of the panels. The elevator is placed in a corner between two structural walls, but the other two walls of the elevator shaft are non-structural partition walls. As stated above, the stairs are only partially connected to the structural system, therefore their contribution to the global stiffness is irrelevant with respect to the large panels. Also the additional walls of the elevator shafts are non-structural walls and do not provide additional stiffness. In conclusion, both the stairs and the elevator shaft will be taken into account only as masses in the numerical modelling of the four buildings.

# Chapter 3

## Experimental ambient vibration analysis

### 3.1 Measurement set-up and data pre-processing

Seismic stations were installed in the four selected buildings in order to record ambient vibrations. The stations comprised a 24 bit DSS-CUBE3 digitizer (<http://www.omnirecs.de/>) and a 4,5 Hz three components geophone (see Figure 3.1). The sampling rate was 400 Hz and a build-in GPS antenna provided the timing for the data collection. Since the GPS reception could be missing during the measurements inside the buildings, all stations were activated and left outside for some time before and after the installation, in such a way that GPS time could be synchronized and used to correct time delays with a built-in software after the measurements. Forty stations were available, but a variable number was installed in the buildings, since they had to be placed in private apartments. For all four buildings, one station was installed outside as a reference station, in order to have a recording independent from the building's influence. The installation setting foresaw a

station in every corner of each floor, including the roof, and two stations installed in the basement. This setting is optimal for obtaining information about the global behaviour of the building. As already mentioned, it was not possible to have this ideal condition in all buildings. Tables 3.1-3.4 report the actual setting for each building. The stations were usually recording during one night in each building, hence data was collected for some hours. The measurements are taken along three components, oriented as a Cartesian coordinate system. The first component is aligned with the longitudinal dimension of the buildings' section in plane (x), the second with the transverse one (y) and the third with the building vertical dimension (z) (see also Figures 2.2-2.4 for reference). The recordings was saved in a CUBE property format, which was then converted into the standard miniSEED format. In each miniSEED file the velocity at the measurement position is saved together with the corresponding time at discrete time-steps of 0,0025 s.

Table 3.1: Station positions for the measurements in building 37. The positions A, B, C and D are shown in Figures 2.2-2.4. The numbers in the columns are the stations' ID. Stations that ran out of battery power during the measurements are written in brackets.

Floor	A	B	C	D
Roof	793	797	801	604
9	-	-	(798)	(605)
8	-	-	712	796
7	-	-	-	-
6	-	-	(887)	-
5	900	790	888	(711)
4	-	-	710	(807)
3	799	800	792	875
2	808	809	795	902
1	805	806	713	804
Basement	(802)	(803)	-	-





Figure 3.1: Typical station used for the ambient vibration measurements. The yellow instrument is a 4,5 Hz three components geophone, while the black box is a 24 bit DSS-CUBE3 digitizer. The numbers reported in Tables 3.1-3.4 are the ID of the digitizer.

Table 3.2: As in Table 3.1 but for building 43.

Floor	A	B	C	D
Roof	710	873	809	(807)
9	713	712	-	-
8	796	902	805	711
7	808	900	865	903
6	800	799	-	-
5	791	605	604	795
4	-	-	-	-
3	(901)	(874)	(793)	(797)
2	-	-	804	798
1	891	864	801	790
Basement	898	899	-	-

Table 3.3: As in Table 3.1 but for building 25.

Floor	A	B	C	D
Roof	801	802	798	876
9	808	807	(710)	791
8	(874)	712	805	711
7	(901)	809	865	792
6	-	-	898	875
5	891	804	864	713
4	891	804	864	713
3	604	806	793	899
2	797	796	873	605
1	-	-	899	790
Basement	803	903	-	-

Table 3.4: As in Table 3.1 but for building 4/1.

Floor	A	B	C	D
Roof	710	604	900	902
9	797	801	792	808
8	805	798	713	796
7	-	-	-	-
6	898	876	800	793
5	-	-	807	799
4	874	795	711	804
3	864	888	-	-
2	865	899	903	712
1	891	873	791	875
Basement	-	-	802	803

## 3.2 Spectral analysis

### 3.2.1 Methodology

The first analysis made on the data set was aimed at computing the Fourier spectra of each measured component for all buildings. The Fast Fourier Transformation (FFT) is a technique, based on the Fourier series, that allows an aperiodic time signal  $g(t)$  be described by the linear combination of a given number of periodic functions. Each of these functions has a given frequency ( $\omega = 2\pi \cdot f$ ) and is multiplied by a Fourier coefficient, computed with (3.1).

$$G(\omega) = \int_{-\infty}^{\infty} g(t)e^{-i\omega \cdot t} dt \quad (3.1)$$

$G(\omega)$  is the Fourier coefficient for the frequency  $\omega$ . From the set of Fourier coefficients, it is possible to define the set of periodic functions describing the signal. The Fourier coefficients are complex values: for each frequency component, the modulus is the amplitude of the periodic function and the ratio between the real and the imaginary part is the phase shift that has to be taken into account in the periodic function. The Fourier spectrum is graphically represented by the plot of the spectral amplitude in the frequency field.

In our application, the time signal is discrete with a sampling rate equal to 400 Hz. This implies a limitation in the frequency range that can be considered in the spectrum. The Nyquist frequency,  $f_N$ , sets the upper boundary of the frequency that can be computed by the numerical processing of the signal, and is defined as half of the sampling rate, as in (3.2), where  $n$  is the

number of samples in the time interval  $T$ .

$$f_N = \frac{n}{2T} > \max f \quad (3.2)$$

If a finite number  $N$  of frequencies are considered for the spectrum, the method is called Discrete Fourier Transform (DFT), based on the FFT algorithm. In this case, the Fourier coefficients are computed with a sum as in (3.3).

$$G_n = \frac{1}{N} \cdot \sum_{k=0}^{N-1} g_k \cdot e^{-i \cdot 2\pi \cdot \frac{kn}{N}} \quad (3.3)$$

The process implies a discretization of the signal, which has to be sampled at  $N$  points to obtain the values of  $g_k$ . The number of samples has to be a power of two. The maximum number of samples is limited by the time window used for the data collection. It is worth noting that it is very important to select a significant frequency range for the operation, covering those values that have the higher energy content in the time signal.

FFT and DFT usually require some preliminary operations on the time signal, in order to avoid misleading results. With the objective of discarding small Fourier coefficients, which are numerical noise with respect to the larger values, a filter is generally applied to the signal, so that some frequencies are not considered in the FFT. Also, in order to avoid spectral leakage, the time windows applied to the signal can be overlapped. Last, but not least, a cosine taper function is applied to the beginning and the end of the recording in order to prevent numerical noise.

### 3.2.2 Analysis

The spectral analysis aims firstly at retrieving the fundamental frequency of the buildings. This is the frequency value corresponding to the first peak of the Fourier spectrum. Higher modes can also be identified in the spectra. In our application, since we have sensors recording on the three components at the same position on different floors, the spectra can also give some information on the modal shape. The input data for the analysis are the recordings over several hours. For building 43, five hours were considered, from 24:00 to 05:00 local time (UTC +6). For building 4/1, we took a four-hour signal, from 01:00 to 05:00 local time. Recordings in buildings 37 and 25 had some corrupted parts, probably due to some machine working in the buildings (elevator, washing machine) or to someone moving the sensor. Therefore, only three hours were considered for building 37, from 11:00 to 14:00 and two hours, from 24:00 to 02:00, for building 25. Different time-windows were used for the four buildings because the recording time varied from one building to the other. Moreover, in the data processing, the times window was chosen so that most sensors were recording, because some of them lost battery power during the measurements.

The data were processed with a bandpass Butterworth filter, designed to discard all frequency content above 100 Hz and below 0,2 Hz: this range excludes from the analysis frequency content that is not significant for the analysis. For the computation of the DFT, a finite number of points were sampled from the signal, equal to  $N = 2^{16} = 65536$ . A cosine taper function was applied to the beginning and the end of the time signal. The FFT was then computed on time windows with a 50% overlap. The average and the standard deviation of the coefficients were then computed.

### 3.2.3 Results

The first frequencies of vibrations for the buildings were estimated, their values and the corresponding modal shape do not vary much among the four buildings, as can be expected from their similar characteristics. Figure 3.2 shows the spectra of recordings for the three components (x, y, z are in blue, red and black respectively) at position A on different floors from the basement (bottom) to the roof (top) for building 43. In Appendix 2, similar plots of the spectra at the four recording positions are reported for all buildings. The amplitude variation along the height in the spectra represents the displacement variation in the modal shape. Looking at the spectra in the three directions on different floors, it is possible to identify flexural modes in x and y from the peaks of these components. Torsional modes can also be identified, because spectra of all components feature a peak at the same frequency. Coupled modes cannot be identified in the spectra.

In Figure 3.2, the right column shows the first three modes, while the left shows the higher modes. The fundamental frequency can be identified at 2,46 Hz with a flexural mode in y. The second and third peak correspond to a flexural mode in the x direction (2,74 Hz) and a torsional mode (2,91 Hz) respectively. In fact, the second peak is only present in the spectra of the x and z component, while the third can be seen in the spectra of all three component. As far as the higher modes are concerned, a torsional mode can be clearly seen on the left at 6,83 Hz. The second flexural mode in the x direction is also visible at 8,00 Hz: it can be seen that the displacement increases, reaches the maximum amplitude, decreases, goes to zero and then increases again.

Some common features can be seen in the spectra for all four buildings: the first peak can always be seen in the spectra for the y component at around

2,5 Hz. The first mode is then identified for all buildings as a flexural mode in the y direction, with a frequency around 2,5 Hz.

Comparing the spectra for building 43 (Figure 3.2) with those for building 37 (Figure 3.3), some differences are noted. In general, the spectra of building 37 shows many more peaks, which can be often related to torsional modes. In the left column of Figure 3.3 the fundamental mode (bending in y) can be identified at 2,42 Hz, together with a first torsional mode (2,51 Hz), a first flexural mode in x (2,73 Hz) and a second torsional mode at 2,82 Hz. Looking at the higher frequencies, only torsional modes can be identified.

A similar pattern can be observed in the spectra of buildings 37, 25 and 4/1 (see Appendix 2). These three building all stand next to another block: this might cause a different dynamic behaviour with respect to building 43.

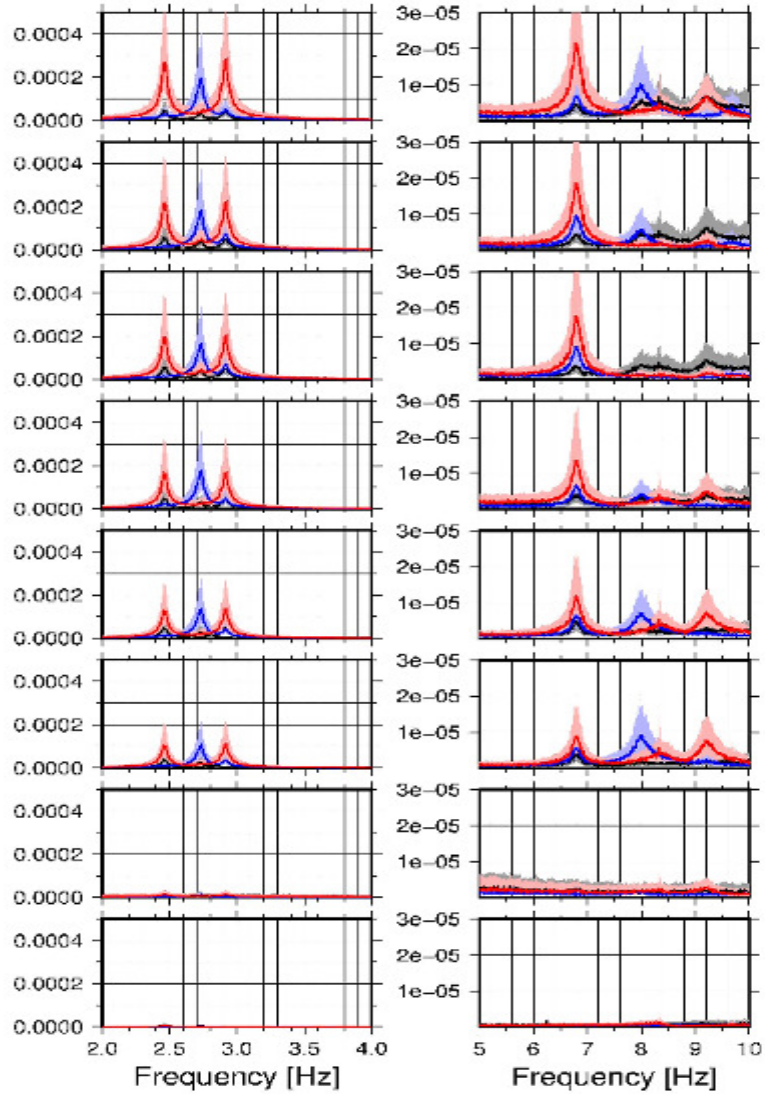


Figure 3.2: Spectra for position A of building 43 at different floors from the basement (bottom) to the roof (top). The x, y and z components are plotted in blue, red and black, respectively. In all spectra, the line represents the mean value and the hues the standard deviation. The fundamental mode (bending in y) is clearly visible on the left at 2,46 Hz. The first bending in x (2,74 Hz) and first torsional mode (2,91 Hz) can also be seen. On the right higher, modes can be identified (torsion at 6,83 Hz, bending in x at 8,00 Hz and torsion at 9,67).



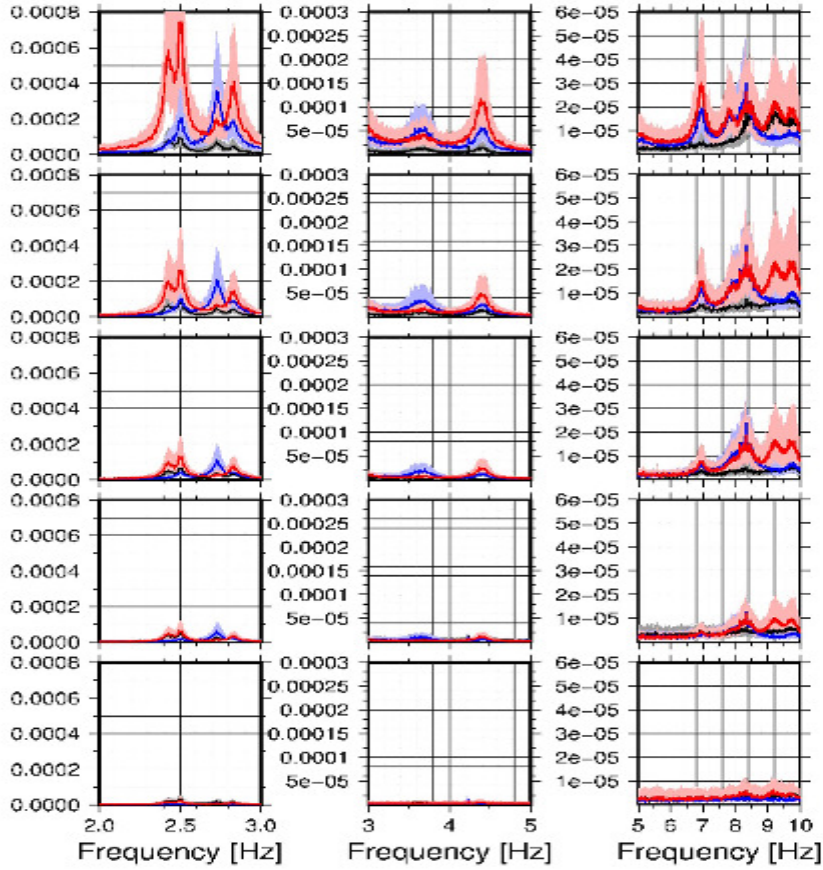


Figure 3.3: Spectra for position A of building 37 at different floors from the basement (bottom) to the roof (top). The x, y and z components are plotted in blue, red and black respectively. In all spectra, the line represents the mean value and the hues the standard deviation. In the spectra on the left, the fundamental mode is clearly visible (bending in y at 2,43 Hz), as well as the first torsional mode (2,51 Hz), the first flexural mode in the x direction (2,73 Hz) and the second torsional mode (2,82 Hz). Torsional modes can be identified in the middle (at 3,60 Hz and 4,41 Hz) and on the right column (6,99 Hz and 8,33 Hz).

## 3.3 Modal analysis with the Frequency Domain Decomposition

### 3.3.1 Methodology

To retrieve the mode frequencies and shapes of the structures from the ambient vibration recordings, a non-parametric identification technique is used, called Frequency Domain Decomposition (FDD, Brincker *et al.* 2001). This method is based on the idea of the Peak Picking (PP) technique (Bendat and Piersol, 1993): the mode frequencies of a system can be estimated from the peaks of the power spectral density (PSD) matrix, as long as the modes are well separated. This condition is no longer necessary in the FDD, which yields exact results if the structure is loaded with white noise, lightly damped and its close modes are geometrically orthogonal. We can state that our case satisfies all these conditions. In the FDD, the PSD matrix of the measurements is first computed: each element of the matrix is the result of the cross-correlation between two Fourier spectra  $f(\omega)$  and  $g(\omega)$ , as written in (3.4).

$$f \cdot g^*(\omega) = \int_{-\infty}^{\infty} f(\omega) \cdot g^*(\omega) d\omega \quad (3.4)$$

Where  $*$  denotes the complex conjugate of the function  $g(t)$ . The recordings used to compute these spectra are the velocity of the structure at a given point, therefore they represent the output of a loading operation, where the input (ambient noise) is unknown. Brincker *et al.* (2001) write:

$$G_{yy}(j \cdot \omega) = \bar{H}(j \cdot \omega) \cdot G_{xx}(j \cdot \omega) \cdot H^T(j \cdot \omega) \quad (3.5)$$

In (3.5),  $G_{yy}(j \cdot \omega)$  is the PSD matrix of the output, a function of the imaginary unit  $j$  and the angular frequency  $\omega$ .  $G_{yy}(j \cdot \omega)$  results from the pre- and post-multiplication of the PSD matrix of the input,  $G_{xx}(j \cdot \omega)$ , with the frequency response function (FRF) of the system,  $H(j \cdot \omega)$ , where the overbar indicates the complex conjugate matrix and the superscript T indicates the transposed matrix. Since the input is white noise, the PSD matrix  $G_{xx}(j \cdot \omega)$  is a constant matrix. The output PSD matrix can be then written as the product of the complex conjugate of the FRF function with a constant and with the transpose of the FRF function. In the FRF, it is possible to identify the mode shape vector  $\phi_k$  and the modal participation vector  $\gamma_k$ .  $\lambda_k$  is the pole used to rewrite the FRF in a pole-residual form:

$$H(j \cdot \omega) = \sum_{k=1}^n \frac{\phi_k \cdot \gamma_k^T}{j \cdot \omega - \lambda_k} + \frac{\bar{\phi}_k \cdot \bar{\gamma}_k^T}{j \cdot \omega - \bar{\lambda}_k} \quad (3.6)$$

In the case of light damping, the residue matrix of the PSD becomes proportional to the mode shape vector. When the frequency  $\omega$  is a mode frequency of the system, the deformed shape of the system is also the shape of the triggered mode. Considering that the PSD matrix is computed through the cross-correlation of the Fourier spectra, it follows that the peak values in the matrix occurs at frequencies that are also mode frequencies of the system. At these frequencies, only the corresponding mode shape will determine the FRF, which means that the only mode shape vector with a non-zero participation factor will be the eigenvector representing the modal shape. This allows us to find the mode shapes of the system through a singular value decomposition (SVD) of the output PSD matrix:

$$\hat{G}_{yy}(j \cdot \omega_i) = U_i S + iU_i^H \quad (3.7)$$

In (3.7),  $U_i$  is the matrix of the singular vectors and  $S_i$  is the diagonal matrix of the singular values. Near a frequency peak one (at maximum two) mode shape is dominating the response of the structure and the row  $u_i$ , corresponding to the mode frequency  $\omega_i$ , estimates the mode shape. It is important to note that the method let us also define mixed modes, since the estimated mode shape can be a combination of more than one eigenmode.

### 3.3.2 Analysis

In our application, the output PSD matrix was computed using recordings on all three components for all positions at all floors over several hours (for specifications, see the time intervals reported in paragraph 3.2.2). Because of the high computational cost of the cross-correlation, the input data were resampled at a frequency of 100 Hz. For the cross-correlation, the input data were detrended and tapered with a cosine function at the beginning and at the end. A bandpass Butterworth filter with boundaries 0,2 Hz and 100 Hz was applied to the signal, discarding the frequency values that are either too low or too high to be significant. The cross-correlation was performed considering the three components of each sensor.

### 3.3.3 Results

A plot of the PSD matrix for building 43 is reported in Figure 3.4. It is possible to read on this graph the frequency values corresponding to the modal frequencies of the structure, which are the maxima of the PSD matrix. The displacements of the instrumented points are also known from the SVD of the PSD matrix. Considering the row of the unitary matrix  $U$  corresponding to the PSD peak value, the modal shape of the structure can also be retrieved. Not only has the fundamental mode of the buildings been retrieved, but also

several higher modes. This report features all eigenmodes found below 10 Hz. A summary of the results is presented in Tables 3.5- 3.8. As far as the description of the modes is concerned, the direction is given considering the system reported in Figures 2.2-2.4. For all buildings, the first mode is triggered around 2,5 Hz and is bending in the y direction. The second mode is a torsional mode and the third flexural in the x direction, except for building 43, whose second mode is bending in the x direction and the third is torsional.

The different dynamic behaviour of building 43 was also observed for higher modes: while the other buildings feature several torsional modes and combined modes with bending and torsion, building 43 only has three higher modes below 10 Hz. The sequence of the higher mode shapes is also the same as in the lower modes. These differences might be related to the fact that building 43 is separate from other buildings.

As mentioned above, for buildings 37, 25 and 4/1, several torsional modes were identified below 10 Hz. Observing the modal shapes, it is clear that the adjacent block has great influence on the dynamic behaviour of these buildings. In the first torsional mode shape of all three buildings (frequency is around 2,5 Hz) it can be seen that one side has larger displacements with respect to the other, which is almost in the original position. The torsion should then involve both blocks and the centre of rotation can be identified in the seismic joint between the two. Also, in the higher modes, the fact that most bending modes are combined with torsion could be related to the interaction with the other block.

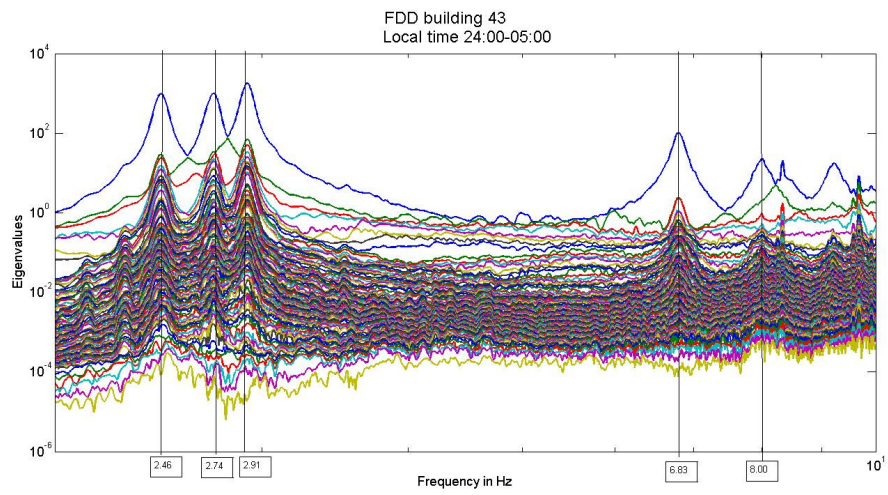


Figure 3.4: Plot of the PSD matrix for building 43. The maximum eigenvalues are present at frequency values that are also the modal frequencies of the structure. In this example, the first three modes can be seen below 3 Hz, together with the higher modes above 6 Hz.

Table 3.5: Results of the modal analysis for building 37. Eight modes were identified below 10 Hz. The first three modes (bending in y, torsion and bending in x) can be seen below 3 Hz. Higher modes are either torsional or combined modes (bending and torsion).

Mode	Frequency [Hz]	Modal shape	Plot of the modal shape
1	2,42	First flexural mode in the y direction	
2	2,51	First torsional mode	
3	2,73	First flexural mode in the x direction	
4	2,82	Second torsional mode	

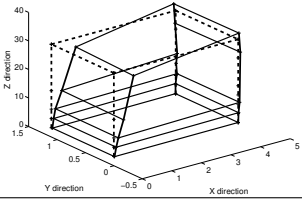
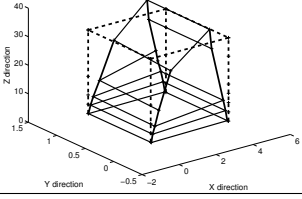
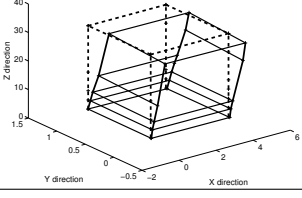
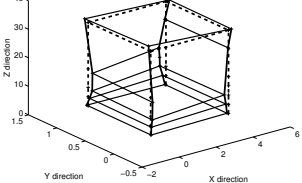
Mode	Frequency [Hz]	Modal shape	Plot of the modal shape
5	3,60	Combined mode: torsion and bending in the x direction	 <p>A 3D wireframe plot showing the modal shape for mode 5. The vertical axis is labeled 'Z direction' and ranges from 0 to 40. The horizontal axes are 'Y direction' (ranging from -0.5 to 1) and 'X direction' (ranging from 0 to 5). The plot shows a rectangular frame with internal lines, exhibiting a combined torsional and bending deformation along the X-axis.</p>
6	4,41	Third torsional mode	 <p>A 3D wireframe plot showing the modal shape for mode 6. The vertical axis is labeled 'Z direction' and ranges from 0 to 40. The horizontal axes are 'Y direction' (ranging from -0.5 to 1) and 'X direction' (ranging from -2 to 6). The plot shows a rectangular frame with internal lines, exhibiting a third-order torsional deformation.</p>
7	6,99	Combined mode: torsion and bending in the y direction	 <p>A 3D wireframe plot showing the modal shape for mode 7. The vertical axis is labeled 'Z direction' and ranges from 0 to 40. The horizontal axes are 'Y direction' (ranging from -0.5 to 1) and 'X direction' (ranging from -2 to 6). The plot shows a rectangular frame with internal lines, exhibiting a combined torsional and bending deformation along the Y-axis.</p>
8	8,33	Combined mode: torsion and bending in the x direction	 <p>A 3D wireframe plot showing the modal shape for mode 8. The vertical axis is labeled 'Z direction' and ranges from 0 to 40. The horizontal axes are 'Y direction' (ranging from -0.5 to 1) and 'X direction' (ranging from -2 to 6). The plot shows a rectangular frame with internal lines, exhibiting a combined torsional and bending deformation along the X-axis.</p>



Table 3.6: Results of the modal analysis for building 43. Six modes were identified below 10 Hz. The sequence of the mode shapes is the same for the lower and the higher modes: bending in y, bending in x and torsion.

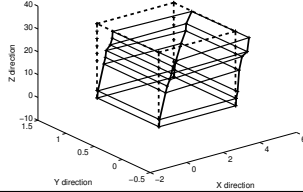
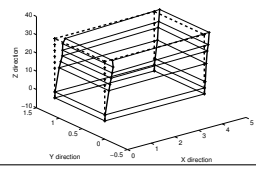
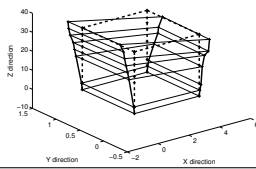
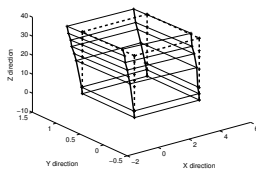
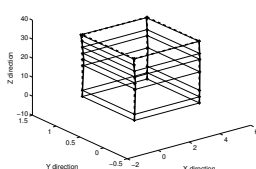
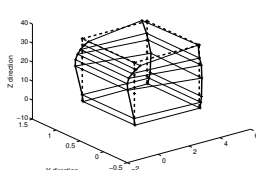
Mode	Frequency [Hz]	Modal shape	Plot of the modal shape
1	2,46	First flexural mode in the y direction	
2	2,74	First flexural mode in the x direction	
3	2,91	First torsional mode	
4	6,83	Combined mode: torsion and bending in the y direction	
5	8,00	Second flexural mode in the x direction	
6	9,67	Second torsional mode	

Table 3.7: Results of the modal analysis for building 25. Six modes were identified below 10 Hz. The first three modes (bending in y, torsion and bending in x) have frequencies below 3,5 Hz. Higher modes are either torsional or combined modes (bending and torsion).

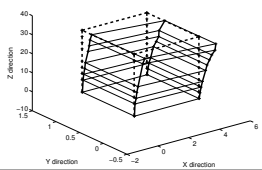
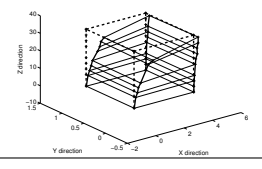
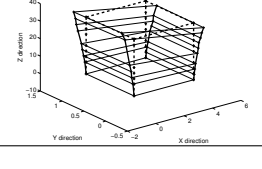
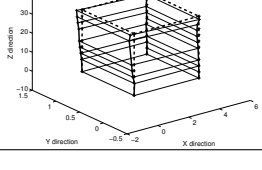
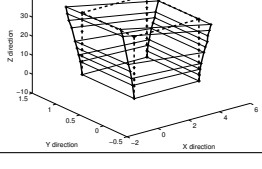
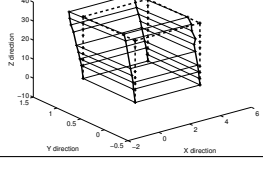
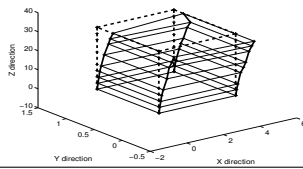
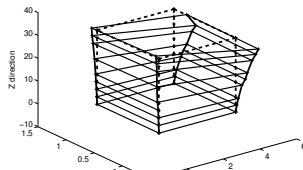
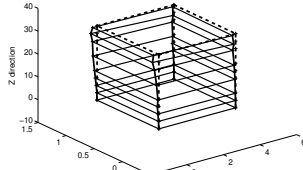
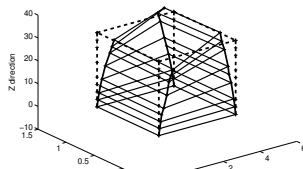
Mode	Frequency [Hz]	Modal shape	Plot of the modal shape
1	2,37	First flexural mode in the y direction	
2	2,51	Combined mode: torsion and bending in the y direction	
3	2,94	First torsional mode	
4	3,47	First flexural mode in the x direction	
5	4,43	Second torsional mode	
6	6,96	Combined mode: Torsion and bending in the y direction	

Table 3.8: Results of the modal analysis for building 4/1. Eight modes were identified below 10 Hz. The first three modes (bending in y, torsion and bending in x) are below 3 Hz. Higher modes are either torsional or combined modes (bending and torsion).

Mode	Frequency [Hz]	Modal shape	Plot of the modal shape
1	2,44	First flexural mode in the y direction	
2	2,59	First torsional mode	
3	2,80	First flexural mode in the x direction	
4	2,93	Second torsional mode	

Mode	Frequency [Hz]	Modal shape	Plot of the modal shape
5	3,39	Combined mode: torsion and bending in the x direction	
6	4,43	Third torsional mode	
7	6,63	Combined mode: torsion and bending in the y direction	
8	8,12	Combined mode: torsion and bending in the x direction	

## 3.4 Interferometric analysis

### 3.4.1 Methodology

#### Deconvolution

Seismic interferometry is a method based on the relationship between waves recorded at different receivers (Snieder and Safak, 2006). Considering an array of sensors recording at the same vertical position on different floors, it is possible to estimate the waves' propagation and their velocity from one position to the other and if they are partly or completely refracted. Knowing this information for a structure means knowing its impulse response function (IRF), which describes how waves propagate within the system.

The technique considers one recording station as a virtual source, called the reference station. Usually, the uppermost or the lowermost station is chosen as this, but the procedure holds for any other station. The idea is to represent the wave propagation as if it was generated by the reference station. To do so, the signal is deconvolved, *i.e.*, its spectrum  $u(\omega)$  at every station is divided by the spectrum at the reference station  $u_{ref}(\omega)$ :

$$D(\omega) = \frac{u(\omega)}{u_{ref}(\omega)} \quad (3.8)$$

In order to avoid instability, an estimate of (3.8) is normally used, where the parameter  $\epsilon$  controls the degree of filtering applied to the deconvolution.

$$D(\omega) = \frac{u(\omega) \cdot u_{ref}^*(\omega)}{|u_{ref}(\omega)|^2 + \epsilon} \quad (3.9)$$

Observing the deconvolved wavefield, it is possible to see how the up- and

down-going waves propagate inside the structure and compute the wave velocity between two stations. The wave velocity is estimated fitting the points obtained by dividing the distance between the considered station and the reference one with the time interval necessary for the wave to travel between the two stations. The time interval is computed as the time shift of the wave positive peaks between the two stations. A least squares fitting of the points in the time-space plane is used to estimate the global wave velocity along the structure. In our case, the recordings on three components allow us to compute both the vertical and two shear wave velocities. Seismic interferometry was first proposed by Kanai (1965) and it has been applied either to earthquake data (Kohler *et al.*, 2007; Picozzi *et al.* 2011) and ambient vibrations (Prieto *et al.*, 2010; Nakata and Snieder, 2014). In our case, the goal is to study the linear IRF of the system as a response to ambient vibration.

## Denoising

In some cases, the up- and down-going waves could not be clearly identified in the deconvolved wavefield, hence a denoising procedure was necessary. The method adopted (Parolai, 2009) was originally meant to be applied to seismograms, but in this case, we applied it to the functions of the deconvolved wavefield. The denoising procedure uses the S transform to obtain a signal with a maximum signal-to-noise ratio, minimizing the loss of information. The S transform is an invertible time-frequency spectral localization technique, combining elements of wavelet transforms and short-time Fourier transforms (3.10).

$$S(\tau, f) = \int_{-\infty}^{\infty} h(t) \frac{|f|}{\sqrt{2\pi}} e^{-(\tau-t)^2 f^2/2} e^{-i2\pi f t} dt \quad (3.10)$$

where  $t$  is the time,  $f$  is the frequency and  $\tau$  is the parameter controlling the position of the Gaussian window on the time axis. Equation (3.10) is applied to a function in time  $h(t)$ , but it can also be rewritten applied to its Fourier spectrum  $H(f)$  (3.11).

$$S(\tau, f) = \int_{-\infty}^{\infty} H(\alpha + f) e^{-2\pi^2 \alpha^2 / f^2} e^{-i2\pi \alpha \tau} d\alpha \quad (3.11)$$

Equation (3.11) is preferred to (3.10) because it is more efficient. A continuous thresholding function (3.14) proposed by Yoon and Vaidyanathan (2004) is applied. The method is applied separately to the real and imaginary part of the S-transform coefficients. The parameter  $\gamma$  is the cut-off value, while  $\alpha$  defines the shape of the function.

$$fc(x) = \begin{cases} x - \text{sgn}(x)(1 - \alpha)\lambda & \text{if } |x| \geq \lambda, \\ 0 & \text{if } |x| \leq \gamma, \\ \alpha\lambda \left(\frac{|x| - \gamma}{\lambda - \gamma}\right)^2 \{(\alpha - 3)\left(\frac{|x| - \gamma}{\lambda - \gamma}\right) + 4 - \alpha\} & \text{otherwise.} \end{cases} \quad (3.12)$$

where  $(x)$  is either the real or imaginary part of  $S(\tau, f)$ . The parameter  $\lambda = \sigma\sqrt{2\log N}$  depends on the frequency-dependent noise variance  $\sigma^2$  and on the length of the signal  $N$ . The three parameters  $\alpha$ ,  $\gamma$  and  $\lambda$  satisfy the conditions  $0 < \gamma < \lambda$  and  $0 \leq \alpha \leq 1$ . In the denoising procedure, the S-transform is first computed. Then the thresholding function is applied to the S-transform coefficients. The signal is finally back-transformed to the time domain with equation (3.13).

$$h(t) = \sqrt{2\pi} \int_{-\infty}^{\infty} \frac{S(t, f)}{|f|} e^{i2\pi ft} dt \quad (3.13)$$

### Computation of the fixed-base frequency

From the results of the interferometric analysis, it is also possible to estimate the fixed-base frequency of the structure  $f_1$  as (3.14).

$$f_1 = \frac{v_s}{4H} = \frac{1}{4\tau_{tot}} \quad (3.14)$$

where  $\tau_{tot}$  is the wave travel-time from the ground floor to the roof,  $v_s$  is the estimate for the average wave velocity in the structure and  $H$  is the height of the building (Trifunac *et al.*, 2010). This frequency is usually different from the one retrieved in the spectral analysis, called  $f_{sys}$ , the fundamental frequency of the soil-structure system.

### 3.4.2 Analysis

In the first step of this analysis, we computed the spectra of several hours of recordings (see Section 3.2.2 for the considered time intervals), with an overlap of 50% and a bandpass filter with boundary values of 0,01 Hz and 20 Hz (Petrovic *et al.*, 2014) and cosine-tapered. For the spectral deconvolution, the regularization parameter  $\epsilon$  is set equal to  $10^{-3}$ , which was identified as the value yielding the best compromise between regularity and loss of information. The station at the top of the building was used as the reference station.

Because the deconvolution on the x component did not have clearly defined peaks, whereas in the y component the up- and down-going waves were easy to identify, the deconvolved signal was denoised using the S transform. The frequency interval considered for the wavelet function is 1-20 Hz and the denoising parameter  $\alpha$  and  $\gamma$  are respectively set equal to 0,7 and 0,5 (Parolai, 2009).



### 3.4.3 Results

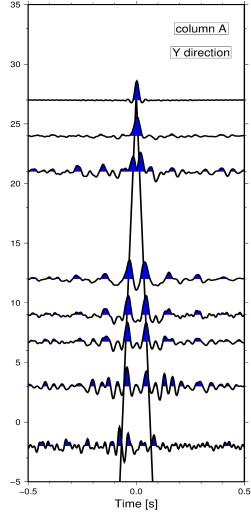
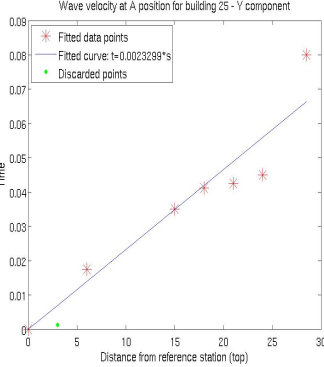
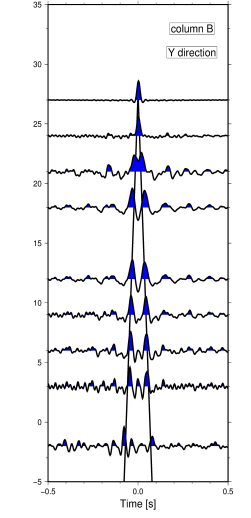
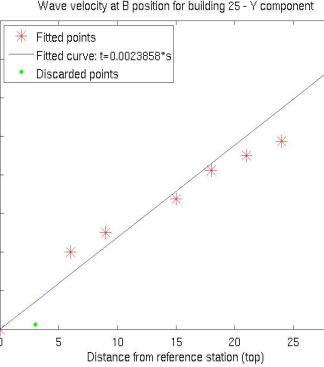
The deconvolution was carried out considering separately the x, y and z components. The results of the deconvolved signal measured in building 25 are reported in Tables 3.9-3.11. In this case, the station on the roof was chosen as reference station. In the same table, the time-distance relation for the up- and down-going wave is reported. The points corresponding to the time when the peak appears in the Green function for the deconvolved wavefield are plotted at their distance from the reference station. These points were used to estimate the wave velocity with a linear least-square fitting of the space-time relation. Some points were discarded in the fitting, because the recording was corrupted or the up- and down-going wave could not be separated. With the fitted space-time relation, an estimate of the wave velocity was computed: the results are reported for all buildings in Tables 3.13-3.16. For the vertical direction, the estimates of the vertical velocity are very scattered: this is due to the fact that the up- and down-going waves could often not be separated in the deconvolution, because their velocity is too high. For this reason, it was not possible to estimate the wave velocity for the z component. The estimate of the average wave velocity is between 350 and 450 m/s for the x component and between 400 and 550 m/s for the y component. These are average estimates on the total height of the buildings.

Table 3.12 shows the results of the deconvolution for the x component before and after the denoise procedure. Looking at the wavefield before the denoising (on the left), the up- and down-going waves cannot usually be identified unequivocally. On the right, the denoised results clearly show the waves propagation on the different floors.

As far as the fundamental fixed-base frequency structure is concerned, the results obtained with Equation (3.14) are reported in Table 3.17 and com-

pared with those obtained for the system with the FDD (Section 3.3.3) . For building 37, the value is overestimated: because the sensor in the cellar did not record properly,  $\tau_{tot}$  in (3.14) is in this case considered equal to the travel time between the ground floor and the roof. The value of  $f_1$  is very close to  $f_{sys}$  for building 43, whereas  $f_1 < f_{sys}$  in the other two buildings.

Table 3.9: Results of the interferometric analysis for building 25, y component. The results of the deconvolution are presented on the left. For this component, the peaks of the up- and down-going waves can be seen separately. On the right the position in time of the peaks are plotted at their distance from the reference station. A space-time relation was then fitted as a least-square interpolation of these points.

Position	Deconvolution (top)	Fit of the wave velocity
A		
B		

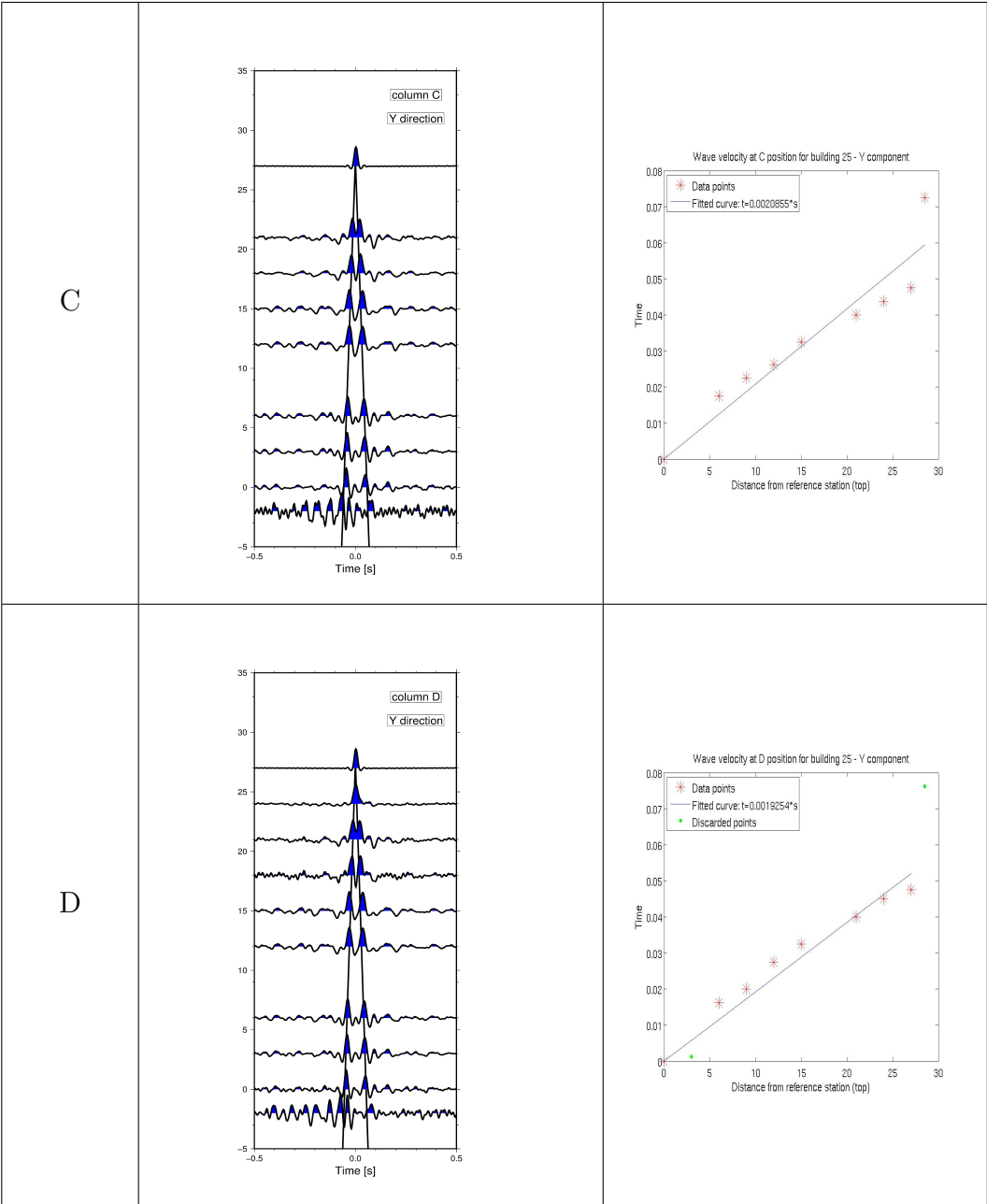
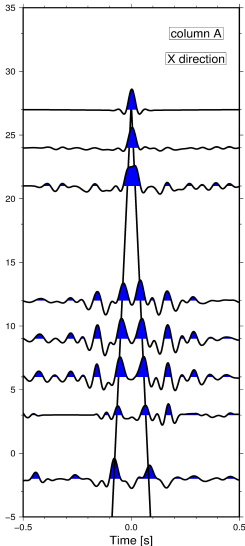
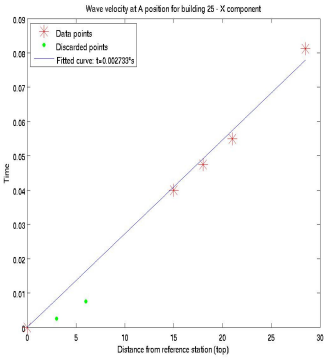
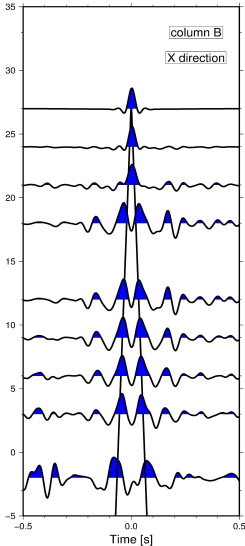
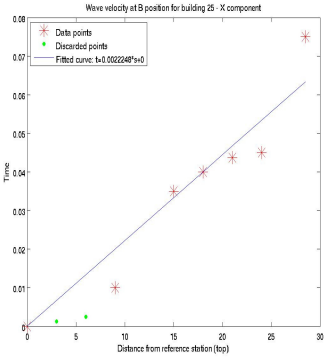
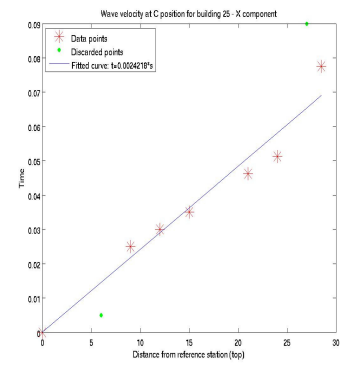
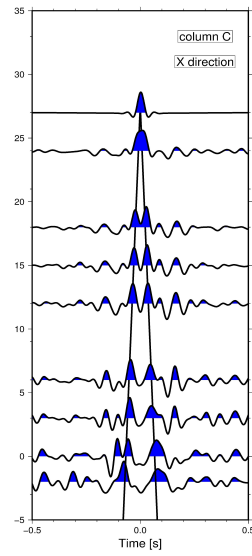


Table 3.10: Results of the interferometric analysis for building 25, x component. The results of the deconvolution are presented on the left. For this component, a denoising procedure was carried out on the deconvolved wave-field for position A, C and D. On the right the position in time of the peaks are plotted at their distance from the reference station. A space-time relation was then fitted as a least-square interpolation of these points

Position	Deconvolution (top)	Fit of the wave velocity
A		
B		

C



D

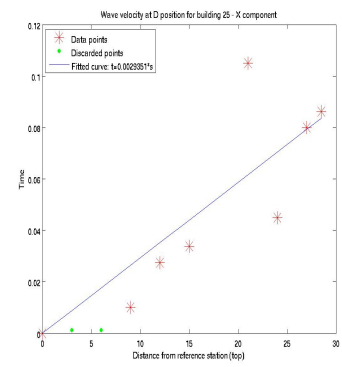
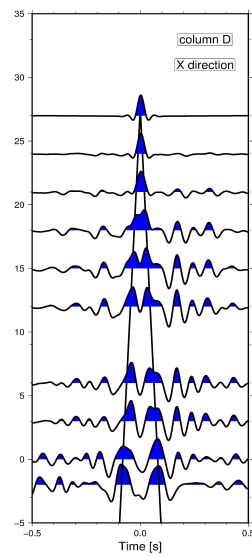


Table 3.11: Results of the interferometric analysis for building 25, z component. For this component, it was not possible to separate the peaks of the up- and down-going waves with the deconvolution, because the wave velocity is too high with respect to the sampling rate adopted. No estimate of the wave velocity can be computed.

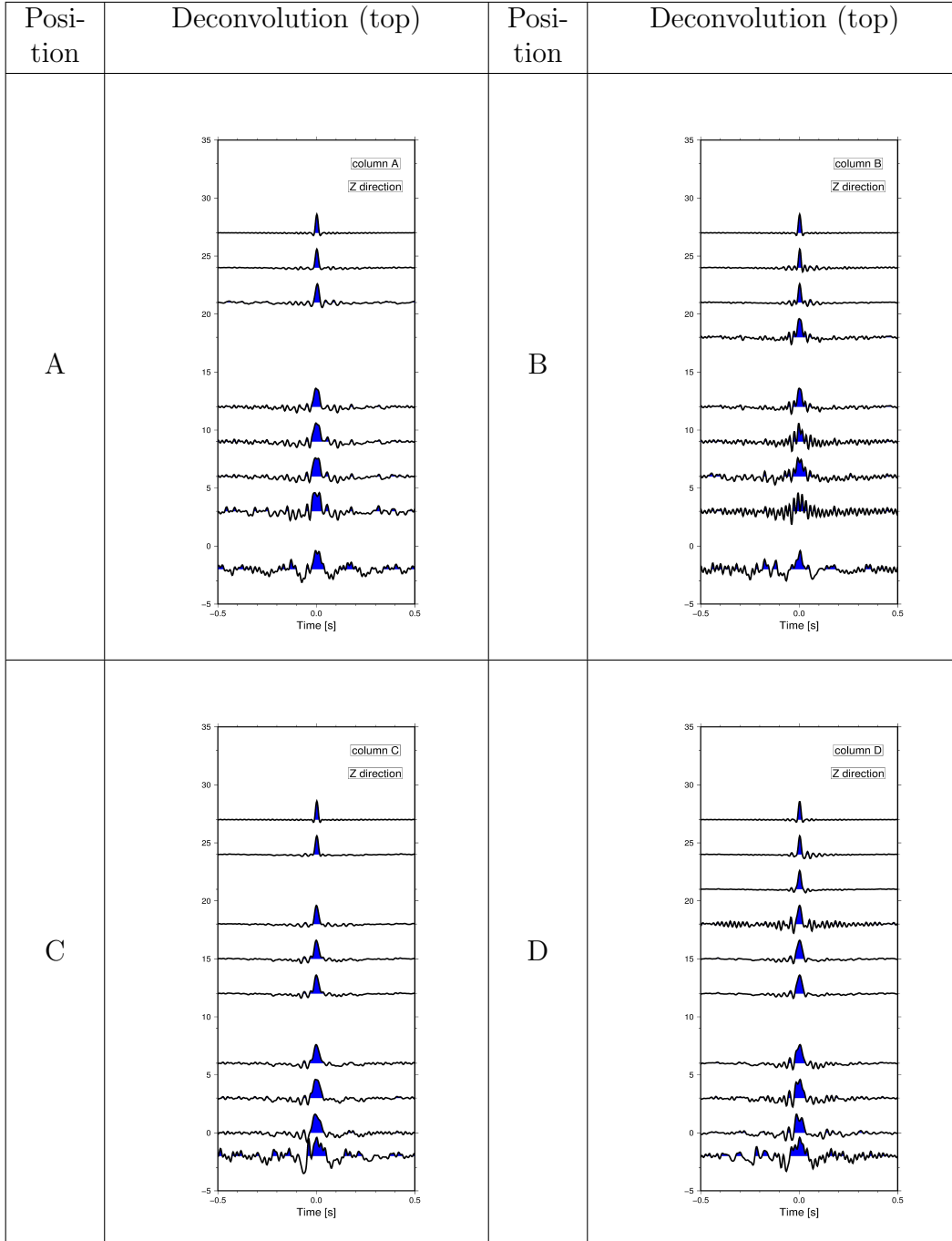
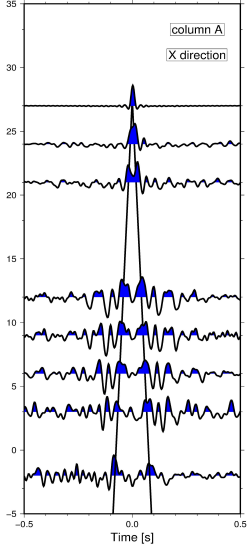
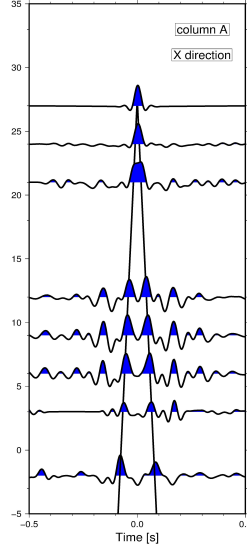
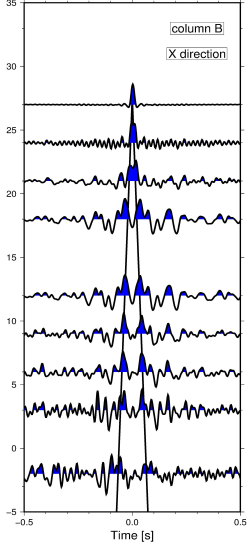
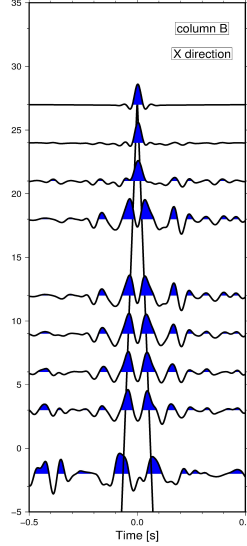


Table 3.12: Comparison between the deconvolved wavefield for the x component before (left) and after (right) the denoising procedure. On the left, the deconvolution results show many peaks: the up- and down-going waves are difficult to identify unequivocally. They can be clearly seen on the right in the denoised wavefield.

Position	Deconvolved wavefield	Deconvolved wavefield after denoising
A		
B		



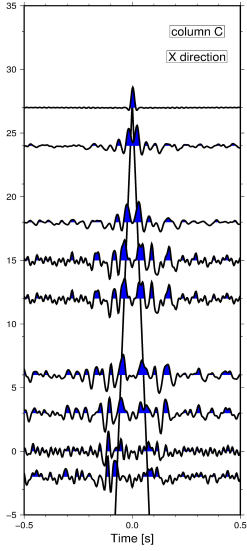
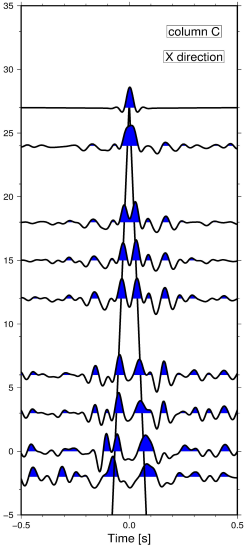
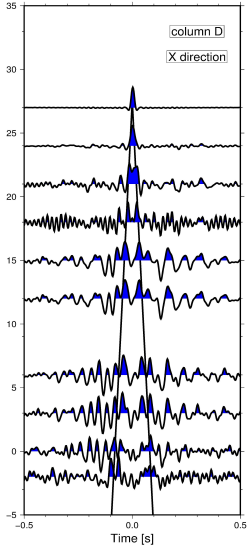
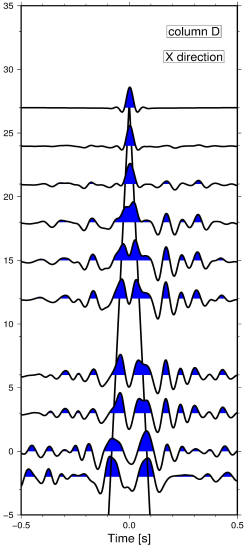
Position	Deconvolved wavefield	Deconvolved wavefield after denoising
C	 <p>The plot shows seismic waveforms for position C. The y-axis represents position from -5 to 35, and the x-axis represents time from -0.5 to 0.5 seconds. A legend indicates 'column C' and 'X direction'. The waveforms are noisy, with a prominent peak at t=0. A dashed line is drawn at approximately y=27.</p>	 <p>The plot shows the denoised seismic waveforms for position C. The axes and legend are the same as in the previous plot. The waveforms are significantly cleaner, with the noise removed, making the primary peak at t=0 much clearer.</p>
D	 <p>The plot shows seismic waveforms for position D. The y-axis represents position from -5 to 35, and the x-axis represents time from -0.5 to 0.5 seconds. A legend indicates 'column D' and 'X direction'. The waveforms are very noisy, with a prominent peak at t=0. A dashed line is drawn at approximately y=27.</p>	 <p>The plot shows the denoised seismic waveforms for position D. The axes and legend are the same as in the previous plot. The waveforms are significantly cleaner, with the noise removed, making the primary peak at t=0 much clearer.</p>

Table 3.13: Estimate of the wave velocity for building 37. The values were obtained through a least-squares fitting of travel times between the pulses of up- and down-going waves at different floors versus the distance of the considered sensor from the sensor on the roof.

Position	y direction [m/s]	x direction [m/s]
A	423	367
B	425	427
C	556	403
D	557	427

Table 3.14: As in 3.13 but for building 43.

Position	y direction [m/s]	x direction [m/s]
A	495	309
B	468	223
C	513	323
D	-	-

Table 3.15: As in 3.13 but for building 25.

Position	y direction [m/s]	x direction [m/s]
A	429	366
B	449	381
C	480	413
D	519	340

Table 3.16: As in 3.13 but for building 4/1.

Position	y direction [m/s]	x direction [m/s]
A	557	411
B	565	256
C	445	331
D	497	392

Table 3.17: Fundamental frequency of the structures. The values computed with the FDD  $f_{sys}$  and the ones retrieved with the deconvolution  $f_1$  are presented.

	$f_1$ [Hz]	$f_{sys}$ [Hz]
Building 37	2,82	2,42
Building 43	2,44	2,46
Building 25	2,21	2,37
Building 4/1	2,11	2,44

# Chapter 4

## Numerical Finite Element modelling

### 4.1 Methodology

#### 4.1.1 Modal Analysis

Numerical modal analysis is a well-known method for structural dynamic analysis (Chopra, 1996), which aims to compute the modal frequencies and forms of multi-degree of freedom (MDOF) systems. Considering a continuous structure as a series of single-degree of freedom (SDOF) systems, it is possible to set up an eigenvalues problem, whose solution describes how the structure vibrates.

The first step is the discretization: a discrete model of the structure is needed to start the computation. In order to obtain a discrete system, it is necessary to assume that mass and stiffness of the structure are concentrated in a finite number of points, instead of being distributed along structural elements. This is usually the most difficult part of the process, because of the several

assumptions that must be made. Indeed making the right choices at this point has a great influence on the results.

Once the discrete MDOF system has been defined, it can be described by two matrixes. The mass matrix  $[M]$  features all the discrete masses present in the model. The stiffness matrix  $[K]$  describes the stiffness relations between the masses. Both are square  $n$  by  $n$  matrixes, where  $n$  is the number of degrees of freedom of the system, which in this case coincides with the number of masses. The MDOF system can then be described by (4.1).

$$[M] \cdot \{\ddot{y}\} + [K] \cdot \{y\} = 0 \quad (4.1)$$

The function  $y$  describes the displacement of the system at each DOF and its second derivative in time the acceleration. The second term of (4.1) is zero because we consider a homogeneous problem, which represents the case of no dynamic load on the structure. If the structure is dynamically loaded, a load function should be present in the second term and the solution of the problem would feature both the homogeneous and the particular solution. The solution will be in any case  $n$ -dimensional, which means that the number of points chosen for the discretization is the maximum number of modes that can be retrieved. It can be noticed that no damping term is present in (4.1). In fact, the dynamic equilibrium for SDOF systems also features damping, as in (4.2).

$$m \cdot \ddot{y} + c \cdot \dot{y} + k \cdot y = f(t) \quad (4.2)$$

where  $c$  is the damping coefficient,  $\dot{y}$  the velocity and  $f(t)$  the applied force. Generally in the modal analysis, the damping term is not explicitly considered, because it is not possible to estimate the damping coefficients for each degree of freedom. Therefore the Rayleigh damping is usually introduced.

This technique consists of estimating two coefficients  $\alpha$  and  $\beta$  that, multiplied by the mass and stiffness matrixes, represent the damping characteristics of the system. Equation (4.3) shows how the damping matrix  $[C]$  is expressed with the Rayleigh damping coefficients.

$$[C] = \alpha \cdot [M] + \beta \cdot [K] \quad (4.3)$$

In this way, damping can be considered in the computation, by simply multiplying the two matrixes by the two coefficients. The values of  $\alpha$  and  $\beta$  are normally chosen to fit the damping behaviour of the system at certain modes. This means that the actual damping behaviour at other modes could be different than that represented by the model and that the results of the analysis would not represent the actual dynamic behaviour of the structure. In (4.1) the function  $\{y\}$  can be described as the product of a spacial term  $\{\phi_j\}$  with a function  $\eta(t)$  that varies with time. Generally,  $\eta(t)$  is a harmonic function of amplitude  $A_j$ , radial frequency  $\omega_j$  ( $\omega_j = 2 \cdot \pi \cdot f$ ) and phase angle  $\phi_j$ . Expression (4.1) can be then rewritten as (4.4).

$$-[M] \cdot A_j \cdot \omega_j^2 \cdot \{\phi_j\} \cdot \sin(\omega_j + \theta_j) + [K] \cdot A_j \cdot \{\phi_j\} \cdot \sin(\omega_j + \theta_j) = 0 \quad (4.4)$$

Simplifying (4.4), it is possible to formulate the eigenvalues problem (4.5).

$$\{[K] - [M] \cdot \omega_j^2\} \cdot \{\phi_j\} = 0 \quad (4.5)$$

The spacial term  $\{\phi_j\}$  is the eigenvector of the problem, representing the modal form, while the eigenvalues  $\omega_j$  represent the eigenfrequencies of the system. The eigenvectors  $\{\phi_j\}$  are linearly independent and orthogonal with respect to the mass and stiffness matrixes. This means that it is possible to

diagonalize the problem with pre- and post- multiplication of the eigenvectors with the matrixes. The results of this operation are namely the modal mass matrix  $[M^*]$  and the modal stiffness matrix  $[K^*]$ . Expression (4.1) can then be rewritten with diagonal matrixes as follow in (4.6).

$$[\Psi]^T \cdot [M] \cdot [\Psi] \cdot [\ddot{\eta}(t)] + [\Psi]^T \cdot [K] \cdot [\Psi] \cdot \eta(t) = [M^*] \cdot [\eta(t)] + [K^*] \cdot \eta(t) = 0 \quad (4.6)$$

where  $\{\Psi\}$  is the modal matrix, whose columns are the modal forms. From this last expression, it is possible to compute directly the mode frequencies of the system as the ratio between the modal stiffness matrix and the modal mass matrix. As said before, the eigenvectors  $\{\phi_j\}$  represent the modal form, but they are not absolute values, therefore they only give a relationship between the displacements of the DOF of the system. Usually the eigenvectors will be normed before presenting them as eigenforms. If the problem is not homogeneous, it can also be diagonalized, introducing the modal load vector  $\{p^*(t)\}$ , as written in (4.8).

$$\{\Psi\}^T \cdot [M] \cdot \{\Psi\} \cdot [\ddot{\eta}(t)] + \{\Psi\}^T \cdot [K] \cdot \{\Psi\} \cdot \eta(t) = \{\Psi\}^T \cdot \{p(t)\} \cdot \{\Psi\} \quad (4.7)$$

$$[M^*] \cdot [\ddot{\eta}(t)] + [K^*] \cdot \eta(t) = \{p^*(t)\} \quad (4.8)$$

The displacements computed with (4.7) are in the modal coordinates and must be multiplied with the modal matrix  $\{\Psi\}$  to be in the physical coordinates.

## 4.2 Analysis

A first step in the numerical analysis was to choose an appropriate number of models to set up. As described in Section 2.1, two types of geometry in plan

can be distinguished, the symmetric (buildings number 37 and 43) and the asymmetric (buildings number 25 and 4/1). While the latter have the same balcony distribution and stand both next to another block, the symmetric in plan buildings have different settings and balcony distributions. According to the experimental results, building 37 has a different dynamic behaviour than building 43 (see paragraph 3.3.3). These reasons led us to believe that building 37 and 43 should be studied with two separate models.

Therefore, three different numerical models were set up: a model for building 37, one for building 43 (see Figure 4.1) and one for the asymmetric in plan buildings (25 and 4/1). In the beginning, we modelled buildings 37, 25 and 4/1 as independent buildings, not considering the fact that another block is present next to them.

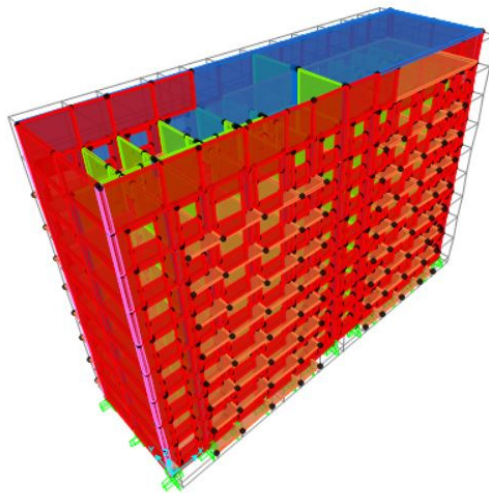


Figure 4.1: 3D view of the model for building 43. The different colors represent the different section types. The roof and the external walls can be clearly seen in blue and red, respectively. Because the view has some transparency, some internal elements can also be seen. The slab elements are presented in orange, and the internal walls in green.



Table 4.1: Assumptions made about the elements' geometry adopted in the models. These dimensions are multiples of the mesh size, equal to 30 cm.

Element	Original size	Size in the model
Window opening in large panels	182x153 cm	180x150 cm
Window opening in small panels	124x153 cm	150x150 cm
Balcony and entrance door in large panels	225x190 cm	240x180 cm
Balcony door in small panels	166x190 cm	150x180 cm
Internal door	125x200 cm	150x180 cm

### 4.2.1 Geometry and mesh size

As reported above (see Section 2.2), the geometry of the structural elements is given. These dimensions were the starting point for choosing a mesh size for the numerical analysis. As a general consideration, a finer mesh leads to more precise results, but could cause the non-convergence of the computation. On the contrary, if the mesh size is too large, the finite element model may not retrieve some of the deformation of the structure. Eventually, the mesh size has to be chosen considering how precise is our knowledge of the geometry. In our case, the dimensions of the structural elements are documented in centimetres, so a very fine meshing is possible. Considering the geometry of the structural elements, a mesh size of 30 cm was adopted. Table 4.1 reports how the dimensions of the structural elements were adapted in the model to be a multiple of the mesh size. The dimensions of the panels were kept as in reality, *i.e.*, 2,7x3,0 m for the small panels, 3,6x3,0 m for the large panels. The balcony span was also considered equal to 1,5 m as in reality. The panels were modelled as shell elements. When an opening is present, four shell elements were used, but their continuity is provided by the mesh. Each area element has been meshed with a maximum size of 0,3 m in both directions and joints were added on the edges when restraints/constraints

exist at adjacent corner points. This means that if two adjacent elements have mesh corners at the same position, a joint connects the two elements. This is ultimately the purpose for having a regular mesh. Four types of area sections were defined:

1. Internal walls: with a thickness of 16 cm;
2. External walls: with a thickness of 30 cm;
3. Slab: with a thickness of 16 cm;
4. Roof: with a thickness of 30 cm.

As discussed above (see Section 2.3), the stairs and elevator shaft will not be modelled. At their positions, a full slab is present. Considering the balconies, we decided to model only their slab, while the vertical walls will be taken into account as masses. This modelling allows us to take into account the real position of their masses. The cantilever length of the balcony is in fact 1,5 m. This model also seemed the most appropriate because the balconies are actually used as interior of the flats and their slab panels continue inside the building.

#### **4.2.2 Materials**

The available information on the materials is quite poor (see Section 2.2): we only know that the cubic compressive strength of the concrete is between 20 and 30 MPa and that the external walls are made of lightweight concrete. After several trials, we saw that lower values of the mechanical characteristics of the materials would provide a better fit to the experimental results. The following materials were defined in the models:

1. Internal walls: concrete with characteristic cylindrical compressive strength of 16 MPa, elastic modulus of 20 GPa and density of 25 kN/m<sup>3</sup>.

2. External walls: concrete with characteristic cylindrical compressive strength of 16 MPa, elastic modulus of 18 GPa and density of 22 kN/m<sup>3</sup>.

3. Slabs and roof: concrete with characteristic cylindrical compressive strength of 16 MPa, elastic modulus of 3000 GPa and density of 25 kN/m<sup>3</sup>.

The last material was defined with such a high value for the elastic modulus so as to allow the slabs be rigid in plan. This means that they would not undergo deformation out of their plane. This assumption is generally true for well-connected horizontal elements. Also, this would avoid retrieving local modal shapes of the balconies, which are not significant for our purposes and cannot be compared to the obtained experimental results.

### 4.2.3 Loads and masses

External loads were applied to the models and considered in the modal analysis as mass sources. First, a distributed area load was computed, to take into account non-structural and accidental loads. As far as the non-structural loads are concerned, the following contributions were identified:

-Lightweight concrete screed (10 cm thick):  $15 \text{ kN/m}^3 \times 0,10 \text{ m} = 1,5 \text{ kN/m}^2$ ;

-Wooden or ceramic floor (5 cm thick, considering an average density of 12 kN/m<sup>3</sup>):  $12 \text{ kN/m}^3 \times 0,05 \text{ m} = 0,6 \text{ kN/m}^2$ ;

-Partition walls: according to the Italian normative (NTC 2008), it is possible to assume an equivalent surface load to take partition walls into account: in our case, a linear weight of 1,10 kN/m is estimated for the partition walls, therefore the equivalent distributed load is equal to 1,20 kN/m<sup>2</sup>.

The non-structural loads sum up to 2,9 kN/m<sup>2</sup>. The accidental distributed

loads are assumed to be equal to  $3 \text{ kN/m}^2$ , based on the Eurocode prescription (EN 1991-1-1) for distributed loads, increased considering that the average surface of a flat is smaller with respect to European standards and therefore the load is more concentrated. The distributed load applied to the slab elements is then  $6 \text{ kN/m}^2$ , input as an area load uniform to frame. This is also applied to balcony slabs because they are mostly closed and used as part of the flats. For the attic slab and on the roof, a reduced distributed load was applied, equal to  $3 \text{ kN/m}^2$ , since no regular non-structural load is present on these two floors.

Then, the mass of the balconies has to be considered. Because of the continuity between the floor and the balcony slabs, this part has been modelled. Therefore, only the loads of the vertical walls are applied to the model. These are estimated as follows:

→ Large balconies: Applied load =  $14,4/2 \text{ kN} + 16,8 \text{ kN} = 24 \text{ kN}$

Lateral wall (full height):  $3 \text{ m} \times 0,16 \text{ m} \times 1,40 \text{ m} \times 25 \text{ kN/m}^3 = 16,8 \text{ kN}$   
(each wall)

Central wall (h= 1 m):  $1 \text{ m} \times 0,16 \text{ m} \times 3,60 \text{ m} \times 25 \text{ kN/m}^3 = 14,4 \text{ kN}$

→ Small balconies: Applied load =  $10,8/2 \text{ kN} + 16,8 \text{ kN} = 22,2 \text{ kN}$

Lateral wall (full height):  $3 \text{ m} \times 0,16 \text{ m} \times 1,40 \text{ m} \times 25 \text{ kN/m}^3 = 16,8 \text{ kN}$   
(each wall)

Central wall (h= 1 m):  $1 \text{ m} \times 0,16 \text{ m} \times 2,70 \text{ m} \times 25 \text{ kN/m}^3 = 10,8 \text{ kN}$

The dimensions of the vertical walls are assumed to be  $1,4 \text{ m} \times 3,0 \text{ m} \times 0,16 \text{ m}$  for the lateral panel and  $2,70 \text{ m} \times 1,00 \text{ m} \times 0,16 \text{ m}$  or  $3,60 \text{ m} \times 1,00 \text{ m} \times 0,16 \text{ m}$  for the front panel of a small and large panel, respectively. The

elements are made of concrete and look like standard panels, so  $25 \text{ kN/m}^3$  is assumed as the density. These loads are applied as point load on the corner joints of the balconies' shells.

As far as the elevator and stair masses are concerned, they are taken into account simply by modelling a full slab in their positions.

### 4.3 Results

A modal analysis was performed for the three models and the results reported in Tables 4.2-4.4. As far as the description of the modes is concerned, the direction is given considering the system reported in Figure 2.2. It can be observed that the three models yield very similar results, in spite of their different geometry. In particular, they all have a fundamental flexural mode in  $y$ , a second mode that is flexural in  $x$  and torsional as third mode. This order well represents the experimental results for building 43, but not for the other three buildings, which have the torsional as the second mode and bending in  $x$  as the third. This will be discussed in more detail in Chapter 5. Considering then the values of the modal frequencies, they are very similar for all three models and are in general higher than those estimated experimentally. All in all, it can be stated that the three models represent structures that appear to display the same dynamic behaviour, which is in contrast with the experimental results.

Table 4.2: Results of the numerical modal analysis for building 37. These initial results were obtained setting up a model according to the information available in the documentation or obtained during the building inspections. The modal shapes are described according to the directions defined in Figure 2.2.

Mode	Frequency [Hz]	Modal shape
1	3,67	Flexural mode in the y direction
2	4,82	Flexural mode in the x direction
3	5,03	Torsional mode

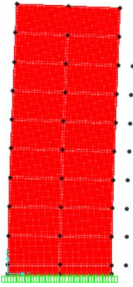
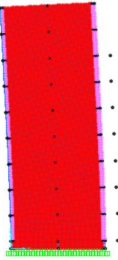
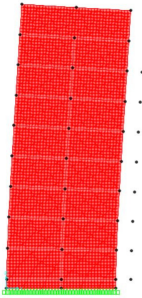
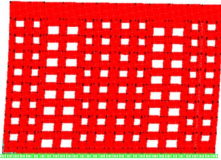
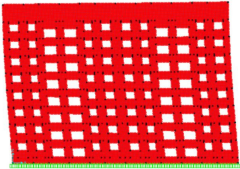
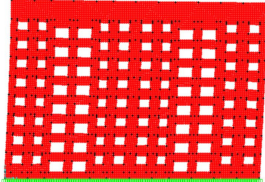
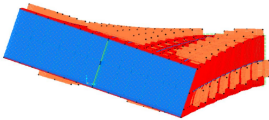
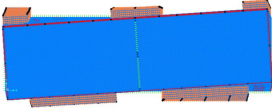
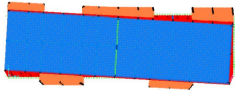
Table 4.3: As in Table 4.2 but for building 43.

Mode	Frequency [Hz]	Modal shape
1	3,76	Flexural mode in the y direction
2	4,95	Flexural mode in the x direction
3	5,32	Torsional mode

Table 4.4: As in Table 4.2 but for the asymmetric buildings (25 and 4/1).

Mode	Frequency [Hz]	Modal shape
1	3,77	Flexural mode in the y direction
2	4,90	Flexural mode in the x direction
3	5,36	Torsional mode

Table 4.5: Pictures of the modal shapes obtained from the numerical models. It can be observed that all three models yield essentially the same modal shapes.

Mode	Building 37	Building 43	Asymmetric buildings
1			
	Flexural mode in y	Flexural mode in y	Flexural mode in y
2			
	Flexural mode in x	Flexural mode in x	Flexural mode in x
3			
	Torsional mode	Torsional mode	Torsional mode

# Chapter 5

## Comparison between experimental and numerical results

In the previous chapters, the experimental and numerical results were presented. We now report them together in Tables 5.1-5.4 in order to compare them. Assuming that the experimental results obtained from the ambient vibration analysis describe the global linear dynamic behaviour of the buildings, the numerical results have to be improved.

We already pointed out that the three models yield very similar results, although they were meant to model different dynamic behaviours. In particular, the fundamental mode, which is bending in y, observed at about 2,4 Hz for all buildings, is well represented in the models, but at a frequency value more than 1 Hz higher than experimentally estimated. The second and third modes computed numerically, *i.e.* bending in the x direction and torsion, respectively, in the ambient vibration analysis were identified as torsion and bending, respectively, for three buildings (37, 25 and 4/1). The order of the



experimental modal shapes is correctly matched only in the case of building 43. The different order of the modal shapes implies that the numerical model does not represent the mass and stiffness distribution of the structure. These properties also govern the values of the modal frequencies, which are higher than the ones obtained experimentally.

In particular, Building 43 differs from the other three in three aspects:

1. It stands clearly separate from other buildings (no seismic joint present).
2. It has a different geometry in plan than buildings 25 and 4/1 (but not building 37).
3. It has a different balcony distribution.

Considering the third aspect, the numerical analysis was also performed without modelling the balcony slabs, which, in this case, were taken into account only as masses. The order of the modal shapes was unchanged. We can therefore conclude that the balcony distribution is not affecting the order of the global modal shapes.

As far as the second point is concerned, the different modal behaviour interests all three other buildings, as they are asymmetric or symmetric in plan. Therefore, only the first aspect is left to consider (see paragraph 6.1.4).

Looking at all four buildings, the eigenfrequency values computed numerically are higher than those obtained experimentally. The poor knowledge on the material properties is pivotal for this aspect. A reduction in the frequency can in fact be obtained assuming that the buildings are characterized by less stiffness or more mass. Following this path, new numerical results were computed and are presented in Chapter 6.

Table 5.1: Comparison between experimental and numerical results for building 37.

Experimental results			Numerical results	
Mode	Frequency [Hz]	Modal shape	Frequency [Hz]	Modal shape
1	2,42	Flexural mode in the y direction	3,57	Flexural mode in the x direction
2	2,51	Torsional mode	4,52	Flexural mode in the x direction
3	2,73	Flexural mode in the x direction	4,75	Torsional mode

Table 5.2: Comparison between experimental and numerical results for building 43.

Experimental results			Numerical results	
Mode	Frequency [Hz]	Modal shape	Frequency [Hz]	Modal shape
1	2,46	Flexural mode in the y direction	3,76	Flexural mode in the y direction
2	2,74	Flexural mode in the x direction	4,95	Flexural mode in the x direction
3	2,91	Torsional mode	5,32	Torsional mode

Table 5.3: Comparison between experimental and numerical results for building 25.

Experimental results			Numerical results	
Mode	Frequency [Hz]	Modal shape	Frequency [Hz]	Modal shape
1	2,37	Flexural mode in the y direction	3,61	Flexural mode in the y direction
2	2,94	Torsional mode	4,80	Flexural mode in the x direction
3	3,47	Flexural mode in the x direction	4,98	Torsional mode

Table 5.4: Comparison between experimental and numerical results for building 4/1.

Experimental results			Numerical results	
Mode	Frequency [Hz]	Modal shape	Frequency [Hz]	Modal shape
1	2,44	Flexural mode in the y direction	3,61	Flexural mode in the x direction
2	2,59	Torsional mode	4,80	Flexural mode in the x direction
3	2,80	Flexural mode in the x direction	4,98	Torsional mode

## Chapter 6

# Calibration of the numerical models

As pointed out in the previous chapter, the numerical results do not match the experimental ones. Assuming that the ambient vibration analysis yields a correct description of the linear dynamic behaviour of the buildings, a calibration of the numerical models was performed. Four different possibilities were considered for the better modelling of the structural behaviour: studying the box-like behaviour of the buildings, assuming a different distribution of the internal walls, changing the elastic modulus of concrete and assuming that the adjacent buildings are actually connected. These are presented in the following paragraphs. Out of these four, two (variation of the elastic modulus and connection between adjacent buildings) were finally adopted to calibrate the numerical models. The results of the calibration are then reported.

## **6.1 Methodologies**

### **6.1.1 Elastic Keys**

As a first possibility to better model the mechanics of the four buildings, we considered that the joints between the panels are peculiar elements, which might not guarantee the box-like behaviour of the structure. We modelled this condition adding a shell element at the end of each vertical wall with particular mechanical properties. This stripe-like shell element, which we called an elastic key, is 30 cm wide and has a different elastic modulus with respect to the walls. Also, an elastic key is placed around the floor slab to model the connection between the horizontal and vertical elements. The Young modulus for the elastic keys is chosen in order to obtain results closer to the experimental ones.

This solution actually represented quite well the global dynamic behaviour of the buildings, but we had to assume very small values of the elastic modulus for the connections. We judged this result unsatisfactory and would in conclusion assume that the joints provide good connection between panels, at least within the elastic regime.

### **6.1.2 Distribution of the internal walls**

Considering how the panels are jointed together and that the distribution of separation elements can vary in private apartments, it is possible to assume a different setting for the internal walls. The distribution we assumed features two additional internal walls running along the longitudinal direction of the buildings, as shown in Figure 6.1. These walls are positioned where the joint between the external panels are present. If these walls were present, the second mode shape would be torsional. However, after the inspection, it

was clear that these walls are not present in the apartments. Also, it would have been very strange if the different dynamic behaviours within the same building series were due to the different position of the internal walls. This option has therefore also been discarded.

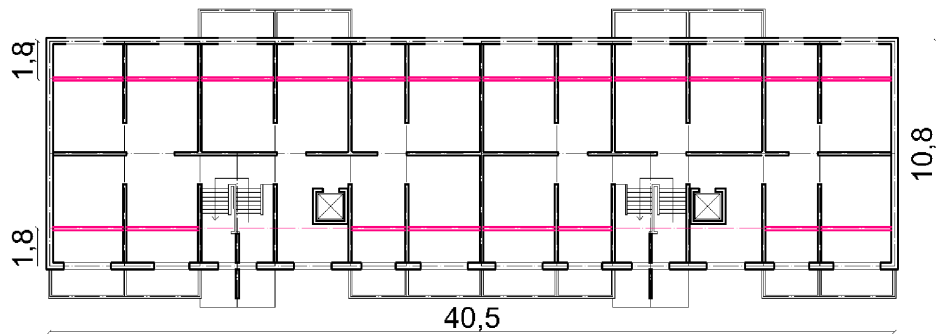


Figure 6.1: Plan view of buildings 25 and 4/1 with the additional longitudinal internal walls (in pink). This different distribution of the internal walls changes the stiffness and masses distribution, so that the order of the modal shapes retrieved numerically is the same as the one obtained experimentally.

### 6.1.3 Material properties

As mentioned before, the documentation on the material properties is very poor, so we decided to vary in the models the material density and elastic modulus to fit the eigenfrequencies of the buildings. This was done for the vertical walls. The values of the parameters are presented in the following section.

It was, however, not possible to find a calibration of the material properties that would yield a correct order of the modal shapes for building 37, 25 and 4/1. Therefore, we excluded the possibility of modelling different buildings with different materials: this would have been also not consistent with the

fact that they all belong to the same series.

#### **6.1.4 Seismic joint**

As we stated in Chapter 5, a significant difference between the buildings could be their position with respect to other buildings. Buildings 37, 25 and 4/1 are separate from another building block only by a seismic joint. This space between the buildings is closed by a metal sheet, so that the wind does not enter. The roof panels are clearly jointed (see Figure 9.4) and at the ground floor a common vertical wall is sometimes present. We do not know if the two buildings are connected at some other points. The local engineers claimed that these joints do not foresee any connection between the two blocks. We modelled different conditions. First, we considered the two buildings being completely connected, as if they were one single building. The result of this modelling was a correct order of the modal shapes. Then, we connected the two buildings only at the points we could see, but the results did not match the experimental ones. Finally, we assumed that the buildings are actually connected by the floor slabs (as in Figures 6.2-6.3). This assumption is motivated by the fact that, although no connection is supposed to exist between the two blocks, the roof slabs are clearly connected.

## **6.2 Analysis**

Out of the four possibilities presented in the previous section, the third and the fourth were adopted in the final modelling.

For all three models, the material properties of the vertical walls were changed.

In the calibrated model we assumed:

1. Internal walls: concrete with characteristic cylindrical compressive

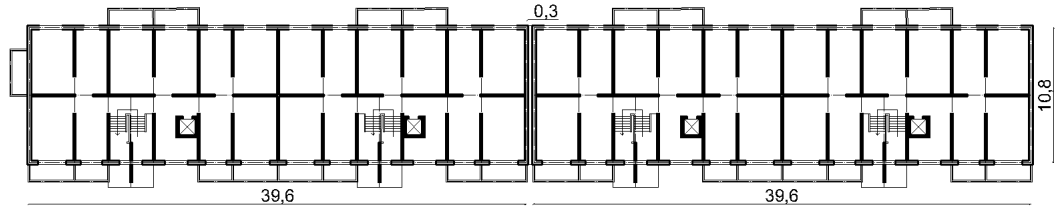


Figure 6.2: Plan view of building 37, showing the adjacent block. In our assumption, a connection 30 cm wide is present between the slabs at each floor.

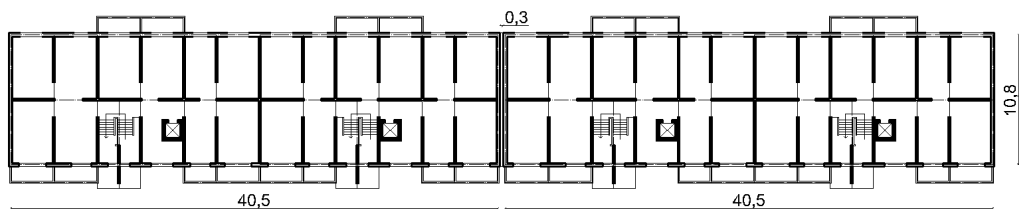


Figure 6.3: Plan view of buildings 25 and 4/1, showing the adjacent block. In our assumption, a connection 30 cm wide is present between the slabs at each floor.

strength of 16 MPa, elastic modulus of 12 GPa and density of 25 kN/m<sup>3</sup>.

2. External walls: concrete with characteristic cylindrical compressive strength of 10 MPa, elastic modulus of 5 GPa and density of 20 kN/m<sup>3</sup>.

The adjacent block is also included in the models of building 37 and of the asymmetric in plan buildings. The two blocks are assumed to be jointed at every floor by a continuous slab. The distance between the two blocks is not constant in reality, but can be approximated to 30 cm in our models, to be consistent with the mesh size. Therefore, in the two models a 30 cm wide slab element connects the two blocks at each floor. A plan view of the two



block-systems is present in Figures 6.2 and 6.3.

### **6.3 Results of the calibration**

The results of the modal analysis for the calibrated models are reported in Tables 6.1-6.4. In the calibrated models, the order of the modal shapes matches the one obtained from the experimental analysis. The percentage error between the frequency values is also reported in the tables. Table 6.5 shows the modal shapes obtained from the numerical analysis. Considering the frequency values, the calibration led to values that are very close to those obtained experimentally. The percentage variation is less than 20% and is null or very close to zero for the fundamental frequency. We cannot actually state that with this calibration we have recovered information about the building materials. We modified the elastic modulus of concrete for vertical walls in order to calibrate the models, but in reality, the concrete could have superior mechanical characteristics and the masses present in the buildings might be higher than what we assumed.

About the order of the modal shapes, it seems very likely that the adjacent blocks have a strong influence on the global dynamic behaviour of the structures. The modal shapes obtained from the numerical modal analysis modelling both blocks are the same as the experimental ones. Even if the assumption we made about the slab connection might be wrong, it is clear that, under dynamic excitation, the two adjacent buildings behave as one structural system.

Table 6.1: Comparison between experimental and numerical results of the modal analysis for building 37. The percentage error is also computed.

Mode	Frequency (experimental) [Hz]	Frequency (numerical) [Hz]	Modal shape	% Error
1	2,42	2,41	Flexural mode in the y direction	10
2	2,51	2,89	Torsional mode	15
3	2,73	3,28	Flexural mode in the x direction	20

Table 6.2: As in Table 6.1 but for building 43.

Mode	Frequency (experimental) [Hz]	Frequency (numerical) [Hz]	Modal shape	% Error
1	2,46	2,43	Flexural mode in the y direction	1
2	2,74	3,18	Flexural mode in the x direction	16
3	2,91	3,39	Torsional mode	16,5

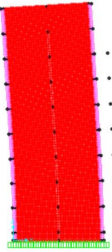
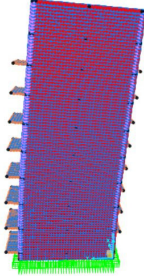
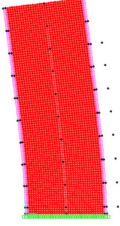
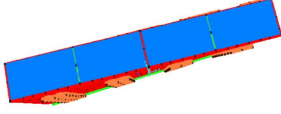
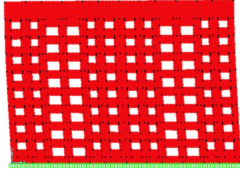
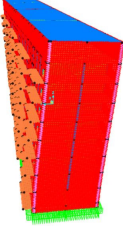
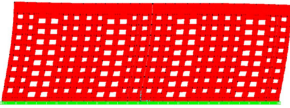
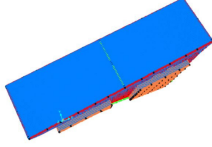
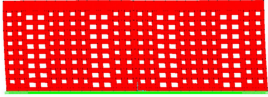
Table 6.3: As in Table 6.1 but for building 25.

Mode	Frequency (experimental) [Hz]	Frequency (numerical) [Hz]	Modal shape	% Error
1	2,37	2,43	Flexural mode in the y direction	2
2	2,94	2,93	Torsional mode	1
3	3,47	3,28	Flexural mode in the x direction	5,5

Table 6.4: As in Table 6.1 but for building 4/1.

Mode	Frequency (experimental) [Hz]	Frequency (numerical) [Hz]	Modal shape	% Error
1	2,44	2,43	Flexural mode in the y direction	1
2	2,59	2,93	Torsional mode	13
3	2,80	3,28	Flexural mode in the x direction	17

Table 6.5: Pictures of the modal shapes obtained from the numerical models. It can be observed that building 37 has a dynamic behaviour very similar to the asymmetric buildings.

Mode	Building 37	Building 43	Asymmetric buildings
1			
	Flexural mode in y	Flexural mode in y	Flexural mode in y
2			
	Torsional mode	Flexural mode in x	Torsional mode
3			
	Flexural mode in x	Torsional mode	Flexural mode in x

# Chapter 7

## Conclusions

### 7.1 Analysis conducted

Experimental ambient vibration analysis and numerical Finite Element modelling were carried out for four r.c. large-panel buildings in Bishkek, Kyrgyzstan. The experimental analysis includes spectral analysis, frequency domain decomposition and interferometric analysis. For the numerical analysis, three different models were set up to study three different global dynamic behaviours that had been identified during the experimental analysis. Then, taking the experimental results as a reference, some changes were made in the numerical models so that their results could be closer to the experimental ones. With the ambient vibration analysis, the modal frequencies and shapes of the four buildings were identified, together with the linear IRF. It was also possible to compute both the fundamental frequency of the fixed-base structure and of the soil-structure system. On the other hand, with the numerical modal analysis, the frequencies and shapes of the buildings were also computed. In the final version of the model, the difference between the experimental and numerical modal analysis is less than 20% and between

0-2% for the fundamental frequency estimate.

## 7.2 Results obtained

Considering the results obtained both experimentally and numerically, two different types of global dynamic behaviour can be identified. On the one hand, building 43, standing separate from other buildings, has three clearly defined modes below 3 Hz (bending in y, bending in x and torsional). On the other hand, the three other buildings, which stand next to another block, have more combined modal shapes involving torsion and a different sequence in the lower modes (bending in y, torsion and bending in x). In conclusion, the buildings in question all have a fundamental flexural mode in the same direction with frequency around 2,4 Hz, but the higher modes are strongly influenced by their standing alone or next to another block.

In the calibration of the numerical model, it was possible to study what aspects mainly influence the global dynamic behaviour of the structures. The relationship between mass and stiffness of the buildings was considered the result of both the material properties and the elements' distribution and mutual connection. The most important conclusion in this sense is that the global dynamic behaviour of the buildings standing next to another block is strongly affected by this condition.

The objective of this work was also to see if one numerical model could represent the behaviour of all four buildings. We can say now that at least two models have to be set up to represent the dynamic behaviour of buildings that stand alone and buildings with an adjacent block. However, if the goal is to obtain the fundamental mode of the building, a single model can be representative for all buildings. It should also be pointed out that the

initial model, based on available information and without taking into account the adjacent buildings, had very different results than the numerical ones, especially with regards to the order of the modal shapes.

### **7.3 Future developments**

In future studies, it should be clearly defined how two adjacent buildings are jointed. The results of ambient vibration analysis on both adjacent buildings could also be useful to identify the modal shapes that involve both blocks. More information about the materials would also lead to an improvement in the numerical models. These could then be used to build structure fragility curves for this type of buildings. Studying a wider number of buildings of this series could also lead to an improvement of the results.

# Chapter 8

## References

- Bendat, J. S. and Piersol, A. G. (1992). Engineering applications of correlation and spectral analysis. (New York: Wiley).
- Bindi D., Mayfield M., Parolai S., Tyagunov S., Begaliev U., Abdrakhmatov K., Moldobekov B., Zschau J. (2011) Towards an improved seismic risk scenario for Bishkek, Kyrgyz Republic. *Soil Dynamics and Earthquake Engineering* 31. 521525.
- Bindi, D., K. Abdrakhmatov, S. Parolai, M. Mucciarelli, G. Gruenthal, A. Ischuk, N. Mikhailova and J. Zschau (2012). Seismic hazard assessment in Central Asia: outcomes from a site approach, *Soil Dynamic and Earthquake Engineering* 37, 8491.
- Brincker, R., L. Zhang and P. Andersen (2001). Modal identification from Ambient Responses using Frequency Domain Decomposition, *Smart Materials and Structures* 10, 441445.
- Chopra, A. K. (1996). Modal analysis of linear dynamic systems: physical interpretation. *Journal of Structural Engineering* 122: 517-527.
- Eurocode 1 (1991). Actions on structures - Part 1-1: General actions - Densities, self-weight, imposed loads fr buildings.



GeoHazards International (1997). Lessons for Central Asia from Armenia and Sakhalin, Stanford, GeoHazards International, 12 pages.

Grünthal, G. (1998): European Macroseismic Scale 1998 (EMS-98). Cahiers du Centre Europeen de Geodynamique et de Sismologie, Volume 15, 99 pp., Luxembourg.

Kohler, M. D., T. H. Heaton and S.C. Bradford (2007). Propagating waves in the steel, moment-frame Factor building recorded during earthquakes, Bulletin of the Seismological Society of America 97, 1334-1345.

Kanai, K. (1965) Some new problems of seismic vibrations of a structure. In: Proceedings of the 3rd world conference on earthquake engineering, Auckland and Wellington, New Zealand.

Molnar, P. and P. Tapponnier (1975). Cenozoic tectonic of Asia: Effects of a continental collision, Science, 189 (4201).

Nakata, N. and R. Snieder (2014). Monitoring a building using deconvolution interferometry, II: Ambient vibration analysis, Bulletin of the Seismological Society of America 104, 204-213.

Norme tecniche per le costruzioni (NTC 2008).

Nurmagambetov, A., N. Mikhailova N and W. Iwan (1999). In: King SA, Khalturin VI, Tucker BE, editors. Seismic hazard of the Central Asia region, in Seismic hazard and building vulnerability in post-Soviet Central Asian republics, Netherlands: Kluwer Academic Publishers, 143.

Parolai S., Orunbayev S., Bindi D., Strollo A., Usupayev S., Picozzi M., Di Giacomo D., Augliera E., Milkereit C., Moldobekov B., Zschau J. (2010) Site effect assessment in Bishkek (Kyrgyzstan) using earthquake and noise recording data. Bulletin of Seismological Society of America 100, 3068-3082.

Parolai, S. (2009): Denoising of Seismograms Using the S Transform. - Bulletin of the Seismological Society of America, 99, 1, pp. 226-234.

- Petrovic, B., Bindi, D., Pilz, M., Serio, M., Orunbaev, S., Niyazov, J., Hakimov, F., Yasunov, P., Begaliev, U. T., Parolai, S. (2015): Building monitoring in Bishkek and Dushanbe by the use of ambient vibration analysis. - *Annals of Geophysics*, 58, 1.
- Petryna, Y., D. Bindi, B. Petrovic, S. Orunbaev, T. Sheraliev, A. Mostbck and U. Begaliev (2014). Dynamic response of buildings in Bishkek using ambient vibration and finite element modeling, *Remote and Ground-based Earth Observations in Central Asia*, dedicated to the 10-year anniversary of CAIAG.
- Picozzi M., Parolai S., Mucciarelli M., Milkereit C., Bindi D., Ditommaso R., Vona M., Gallipoli M.R., Zschau J. (2011) Interferometric analysis of strong ground motion for structural health monitoring: the example of the L'Aquila, Italy, seismic sequence of 2009. *Bulletin of the Seismological Society of America* 101:635651.
- Prieto, G. A., J. F. Lawrence, A. I. Chung and M. D. Kohler (2010). Impulse response of civil structures from ambient noise analysis, *Bulletin of the Seismological Society of America* 100, 23222328.
- Snieder, R. and E. Safak (2006). Extracting the building response using interferometry: theory and applications to the Millikan Library in Pasadena, California, *Bulletin of the Seismological Society of America* 96, 586598.
- Tapponnier, P. and P. Molnar (1979). Active faulting and cenozoic tectonics of the Tien Shan, Mongolia and Baykal regions. *Journal of Geophysical Research*, 84, 3425-3459.
- Trifunac M. D., M. I. Todorovska, M. I. Manic, B. D. Bulajic (2010). Variability of the fixed-base and soil-structure system frequencies of a building - The case of Borik-2 building. *Structural control and health monitoring*, 17, no.2, 120-151.

Ullah, S., D. Bindi, M. Pilz, L. Danciu, G. Weatherill, E. Zuccolo, A. Ischuk, N. Mikhailova, K. Abdrakhmatov and S. Parolai (2015). Probabilistic Seismic Hazard Assessment of Central Asia. *Annals of Geophysics*, 58, 103-124.

Ulomov, V. I. (1999). The GSHAP Region 7 working group. Seismic hazard of Northern Eurasia, *Annali di Geofisica* 42, 1023-38.

Yoon, B. J., and P. P. Vaidyanathan (2004). Wavelet-based denoising by customized thresholding, *IEEE Int. Conf. On Acoustic Speech and signal processing (ICASSP)*, Montreal, May 2004.

Wieland, M., Pittore, M., Parolai, S., Zschau, J., Moldobekov, B., Begaliev, U. (2012): Estimating building inventory for rapid seismic vulnerability assessment: Towards an integrated approach based on multisource imaging. *Soil Dynamics and Earthquake Engineering*, 36, 7083.

World Data Center A for Solid Earth Geophysics (1982). *New Catalogue of strong earthquakes in the U.S.S.R. from ancient times through 1977.*

## Chapter 9

### Appendix 1: Photos of the buildings



Figure 9.1: Front view of building 37.



Figure 9.2: Lateral view of building 37.



Figure 9.3: View of the back of building 37.



Figure 9.4: View of the seismic joint in building 37.



Figure 9.5: Front view of building 43.



Figure 9.6: Lateral view of building 43.





Figure 9.7: View of the back of building 43.



Figure 9.8: Front view of building 25.



Figure 9.9: Lateral view of building 25.



Figure 9.10: View of the back of building 25.



Figure 9.11: View of the seismic joint in building 25.



Figure 9.12: Front view of building 4/1.



Figure 9.13: Lateral view of building 4/1.



Figure 9.14: View of the back of building 4/1.

# Chapter 10

## Appendix 2: FFT spectra

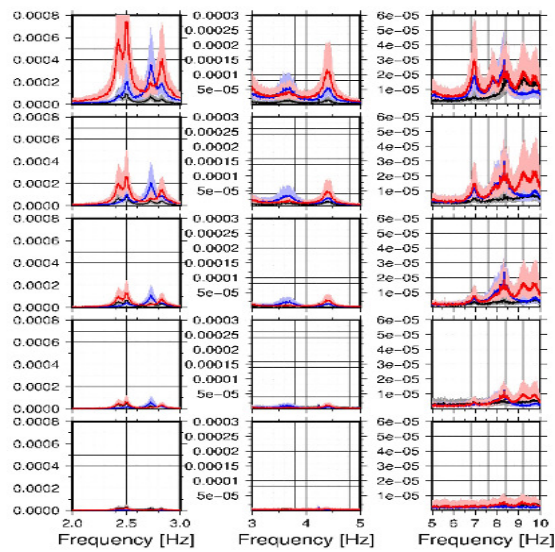


Figure 10.1: Spectra for position A of building 37. The longitudinal, transversal and vertical components are plotted in red, blue and black respectively. In all spectra, the line represents the mean value and the hues the standard deviation.



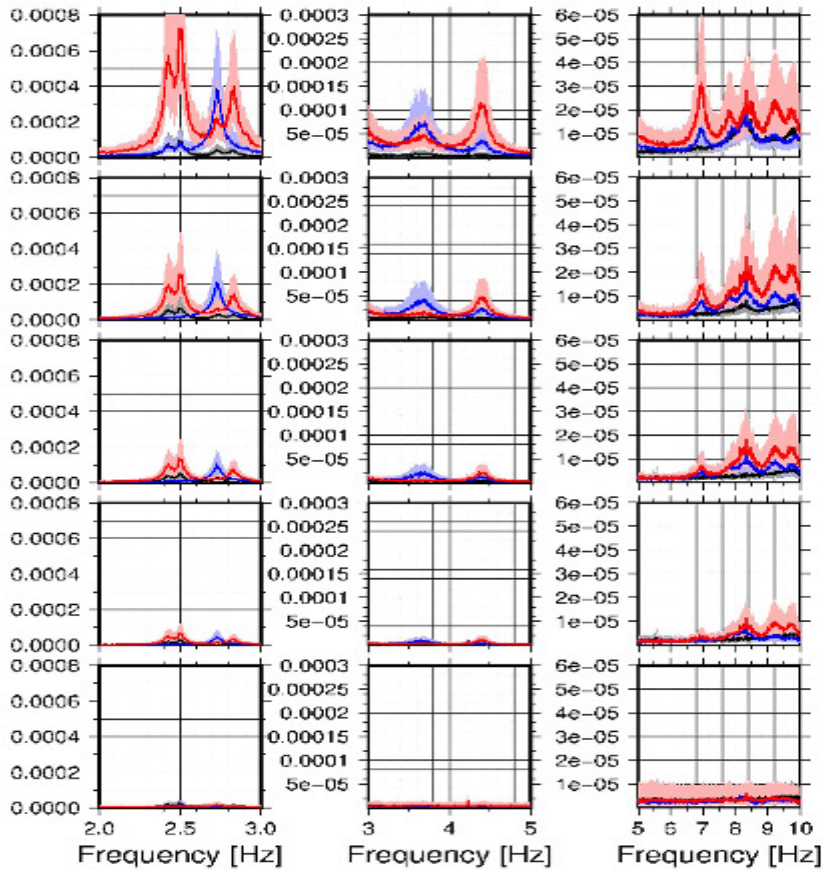


Figure 10.2: Spectra for position B of building 37 at different floors from basement (bottom) to roof (top). The x, y and z components are plotted in blue, red and black respectively. On the left, the first flexural mode in y (2,42 Hz), the first torsional mode (2,51 Hz), the first flexural mode in x (2,73 Hz) and the second torsional mode (2,82 Hz). In the middle column, a combined mode (torsion and bending in y at 3,60 Hz) and the third torsional mode (4,41 Hz) can be seen . Among the higher modes on the right, two combined modes can be identified (6,99 Hz and 8,33 Hz).

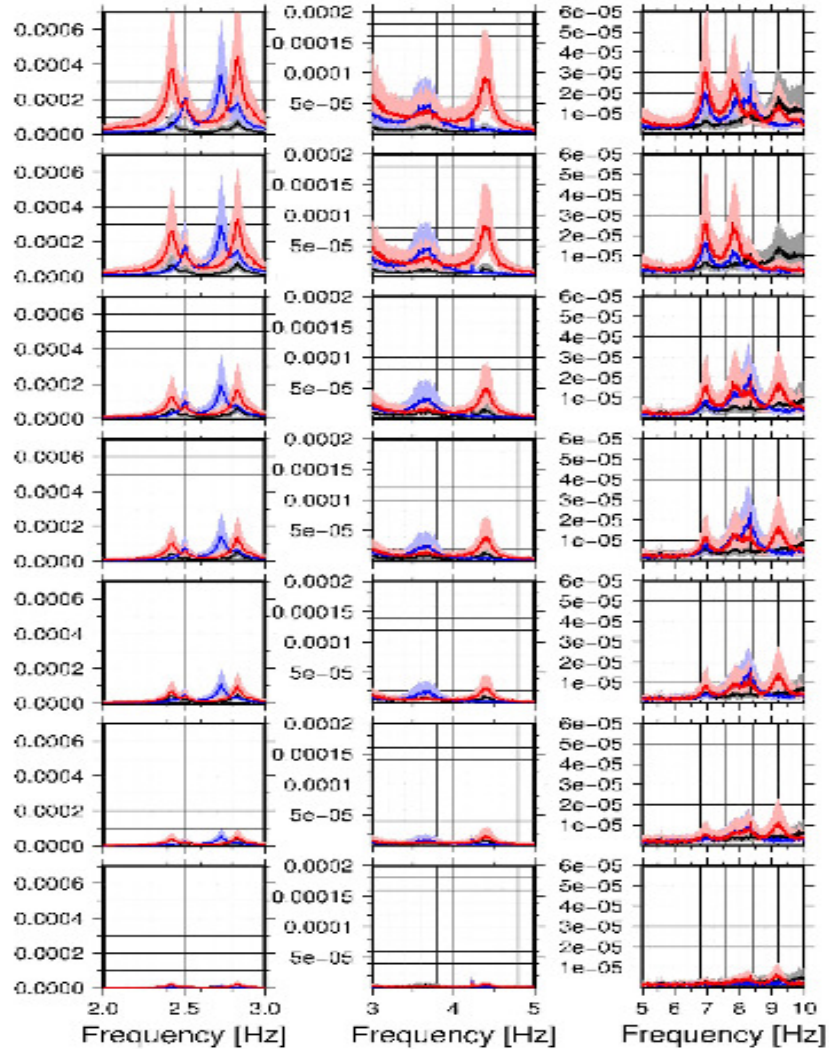


Figure 10.3: Spectra for position C of building 37 at different floors from basement (bottom) to roof (top). The x, y and z components are plotted in blue, red and black respectively. On the left, the first flexural mode in y (2,42 Hz), the first torsional mode (2,51 Hz), the first flexural mode in x (2,73 Hz) and the second torsional mode (2,82 Hz). In the middle column, a combined mode (torsion and bending in y at 3,60 Hz) and the third torsional mode (4,41 Hz) can be seen . Among the higher modes on the right, two combined modes can be identified (6,99 Hz and 8,33 Hz).

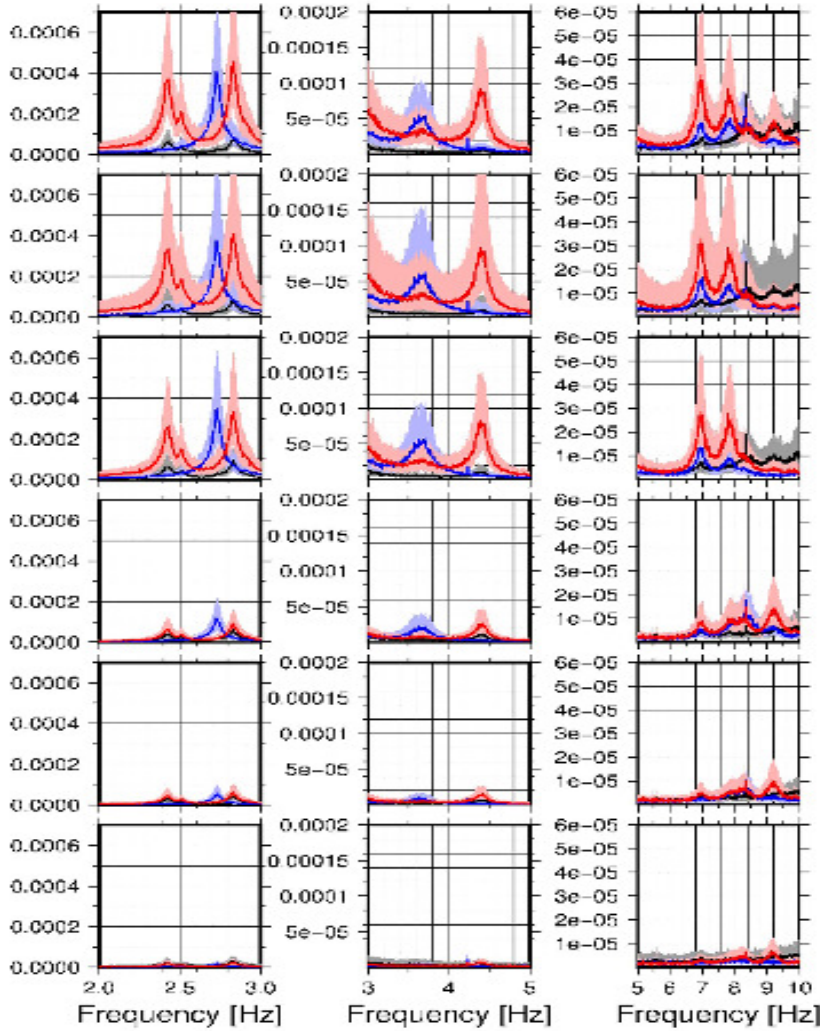


Figure 10.4: Spectra for position D of building 37 at different floors from basement (bottom) to roof (top). The x, y and z components are plotted in blue, red and black respectively. On the left, the first flexural mode in y (2,42 Hz), the first torsional mode (2,51 Hz), the first flexural mode in x (2,73 Hz) and the second torsional mode (2,82 Hz). In the middle column, a combined mode (torsion and bending in y at 3,60 Hz) and the third torsional mode (4,41 Hz) can be seen . Among the higher modes on the right, two combined modes can be identified (6,99 Hz and 8,33 Hz).

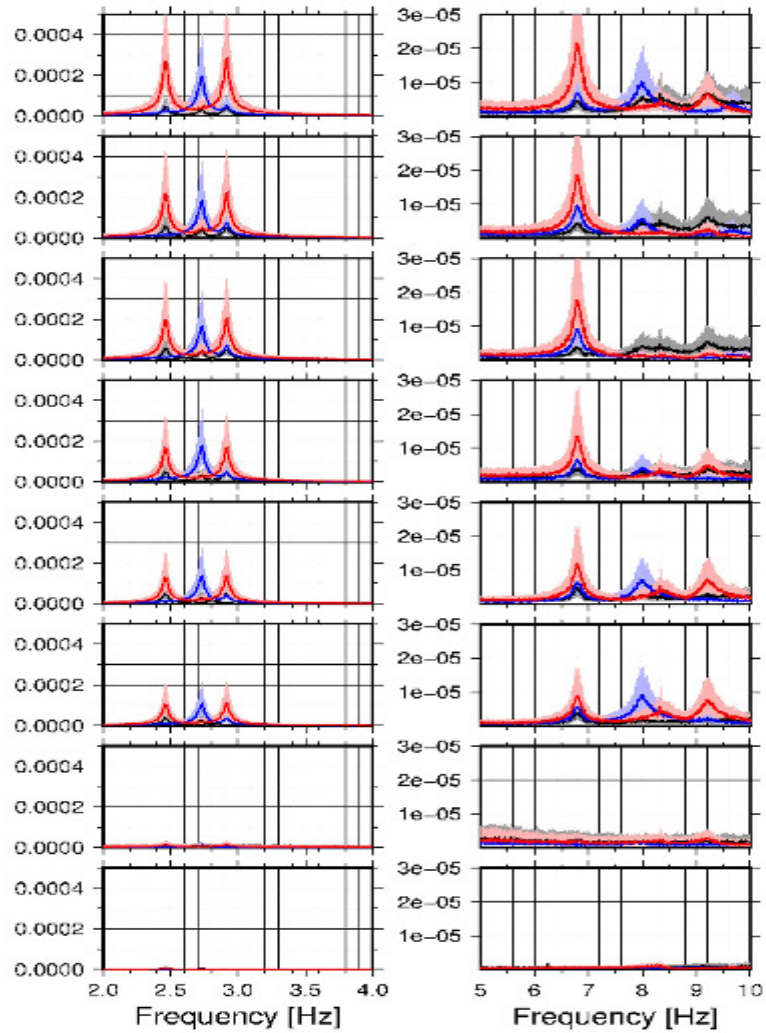


Figure 10.5: Spectra for position A of building 43 at different floors. The x, y and z components are plotted in blue, red and black respectively. On the left the first flexural mode in y (2,46 Hz), in x (2,74 Hz) and the first torsional mode can be identified. On the right a second torsional mode (6,83 Hz) and a second flexural mode in x (8,00 Hz) can be seen.

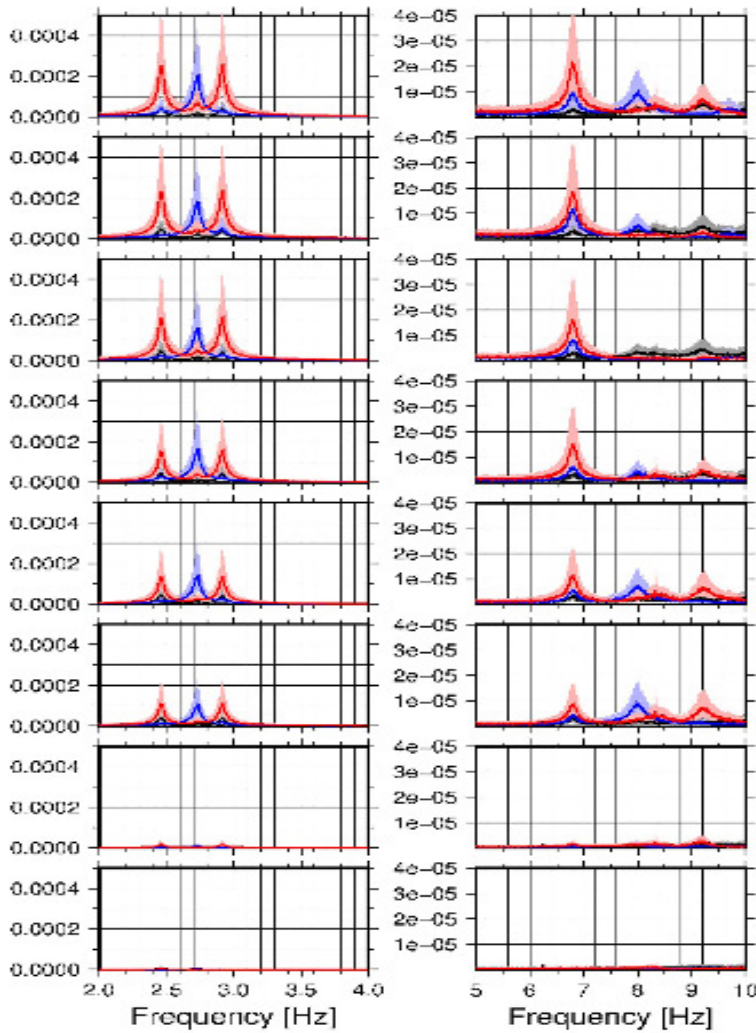


Figure 10.6: Spectra for position B of building 43 at different floors from basement (bottom) to roof (top). The x, y and z components are plotted in blue, red and black respectively. On the left the first flexural mode in y (2,46 Hz), in x (2,74 Hz) and the first torsional mode can be identified. On the right a second torsional mode (6,83 Hz) and a second flexural mode in x (8,00 Hz) can be seen.

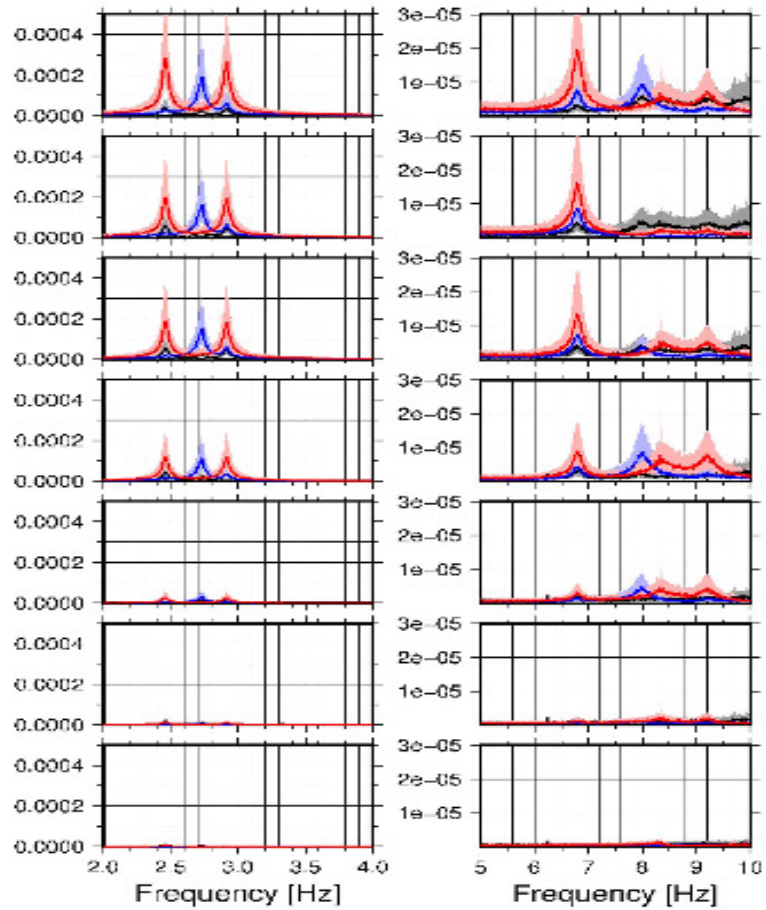


Figure 10.7: Spectra for position C of building 43 at different floors from basement (bottom) to roof (top). The x, y and z components are plotted in blue, red and black respectively. On the left the first flexural mode in y (2,46 Hz), in x (2,74 Hz) and the first torsional mode can be identified. On the right a second torsional mode (6,83 Hz) and a second flexural mode in x (8,00 Hz) can be seen.

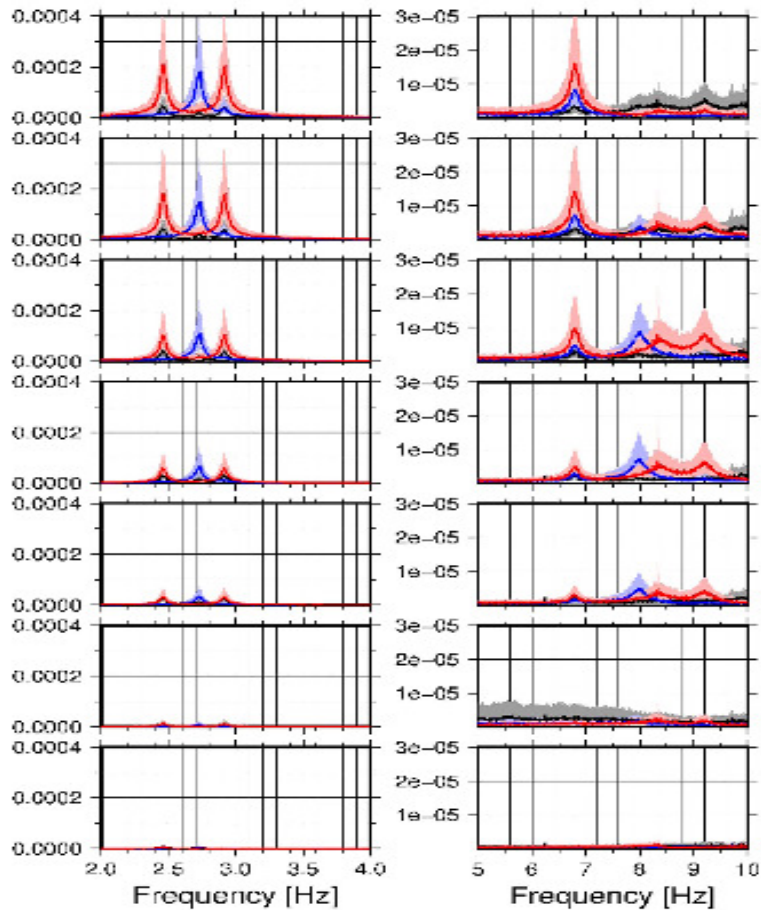


Figure 10.8: Spectra for position D of building 43 at different floors from basement (bottom) to roof (top). The x, y and z components are plotted in blue, red and black respectively. On the left the first flexural mode in y (2,46 Hz), in x (2,74 Hz) and the first torsional mode can be identified. On the right a second torsional mode (6,83 Hz) and a second flexural mode in x (8,00 Hz) can be seen.

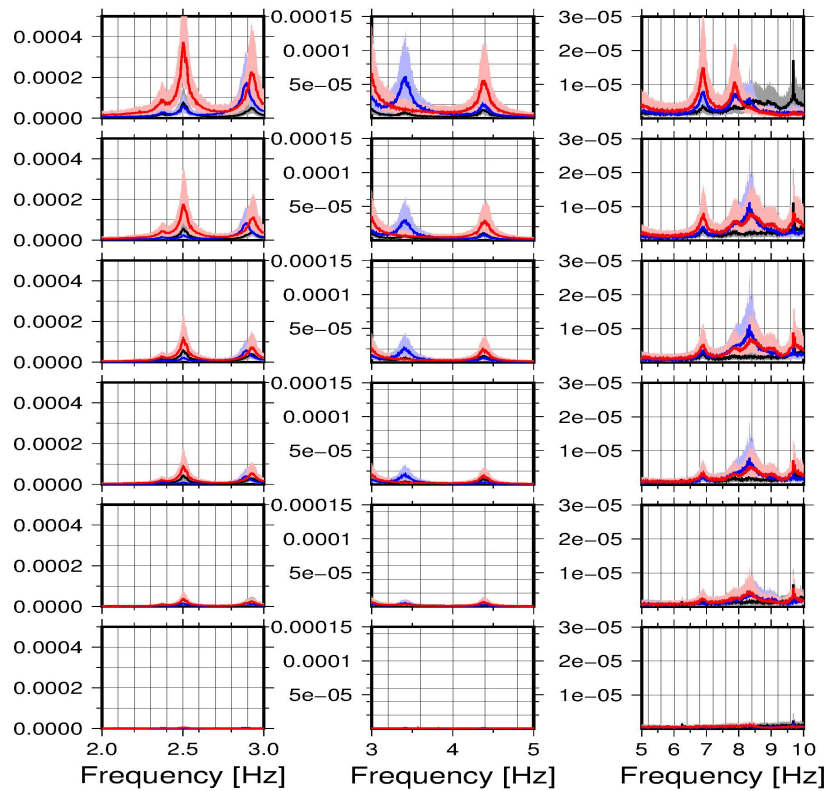


Figure 10.9: Spectra for position A of building 25 at different floors from basement (bottom) to roof (top). The x, y and z components are plotted in blue, red and black respectively. The fundamental mode can be seen on the left (bending in y at 2,37 Hz) very close to a combined mode (2,51 Hz). The first torsional mode (on the right at 2,94 Hz) and flexural mode in x (in the middle at 3,47 Hz) can also be identified. Among the higher modes on the right, two torsional modes can be seen (4,43 Hz and 6,96 Hz).



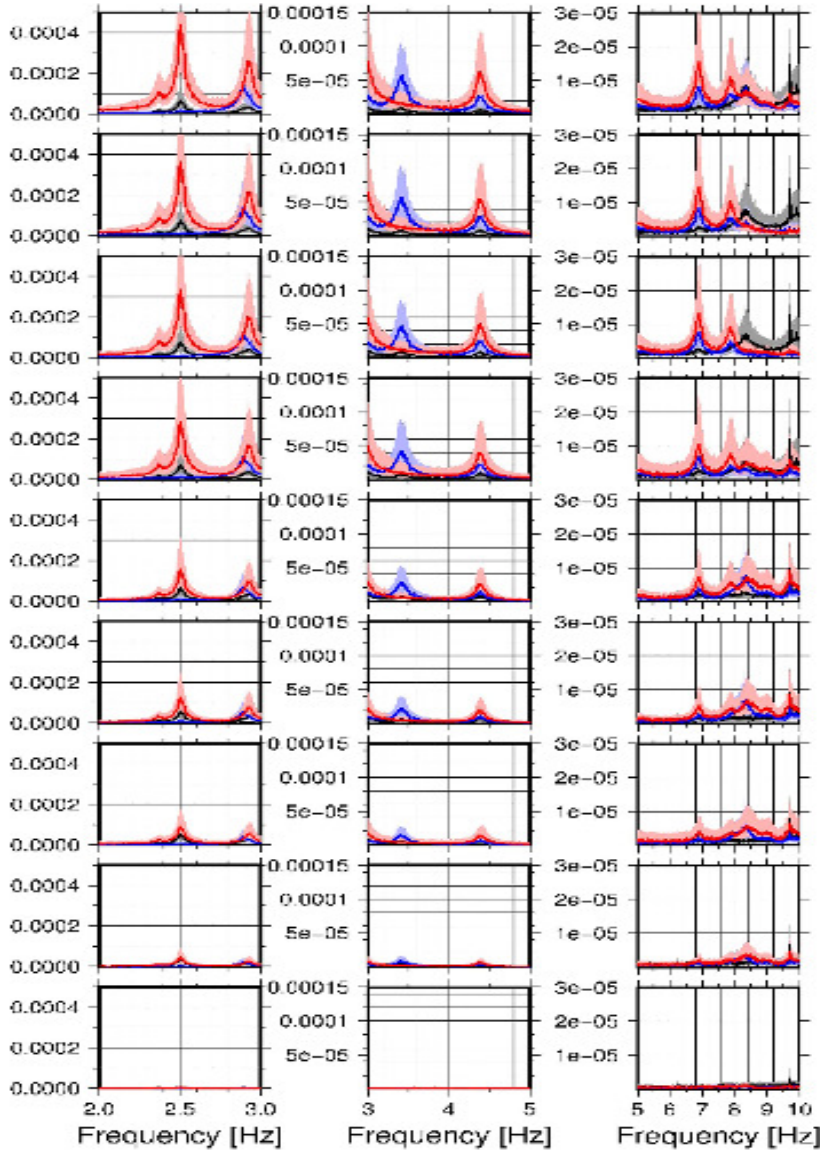


Figure 10.10: Spectra for position B of building 25 at different floors from basement (bottom) to roof (top). The x, y and z components are plotted in blue, red and black respectively. The fundamental mode can be seen on the left (bending in y at 2,37 Hz) very close to a combined mode (2,51 Hz). The first torsional mode (on the right at 2,94 Hz) and flexural mode in x (in the middle at 3,47 Hz) can also be identified. Among the higher modes on the right, two torsional modes can be seen (4,43 Hz and 6,96 Hz).

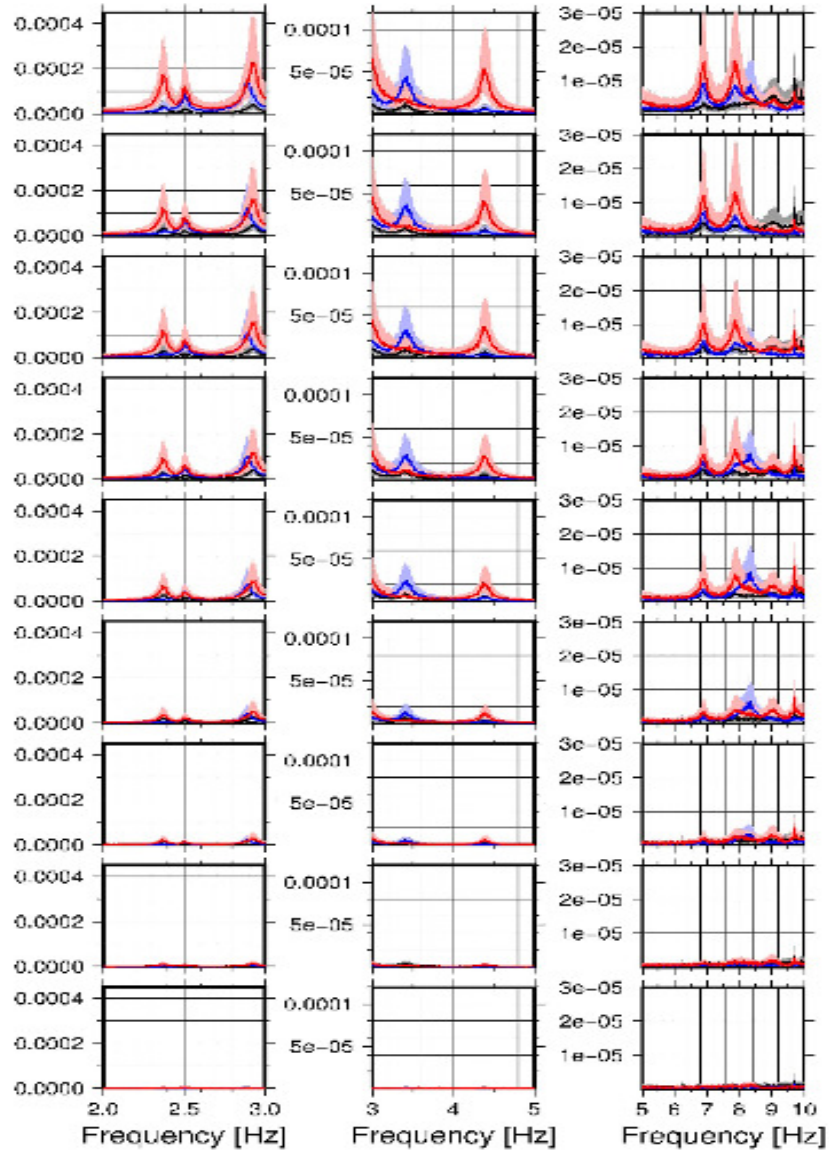


Figure 10.11: Spectra for position C of building 25 at different floors from basement (bottom) to roof (top). The x, y and z components are plotted in blue, red and black respectively. The fundamental mode can be seen on the left (bending in y at 2,37 Hz) very close to a combined mode (2,51 Hz). The first torsional mode (on the right at 2,94 Hz) and flexural mode in x (in the middle at 3,47 Hz) can also be identified. Among the higher modes on the right, two torsional modes can be seen (4,43 Hz and 6,96 Hz).

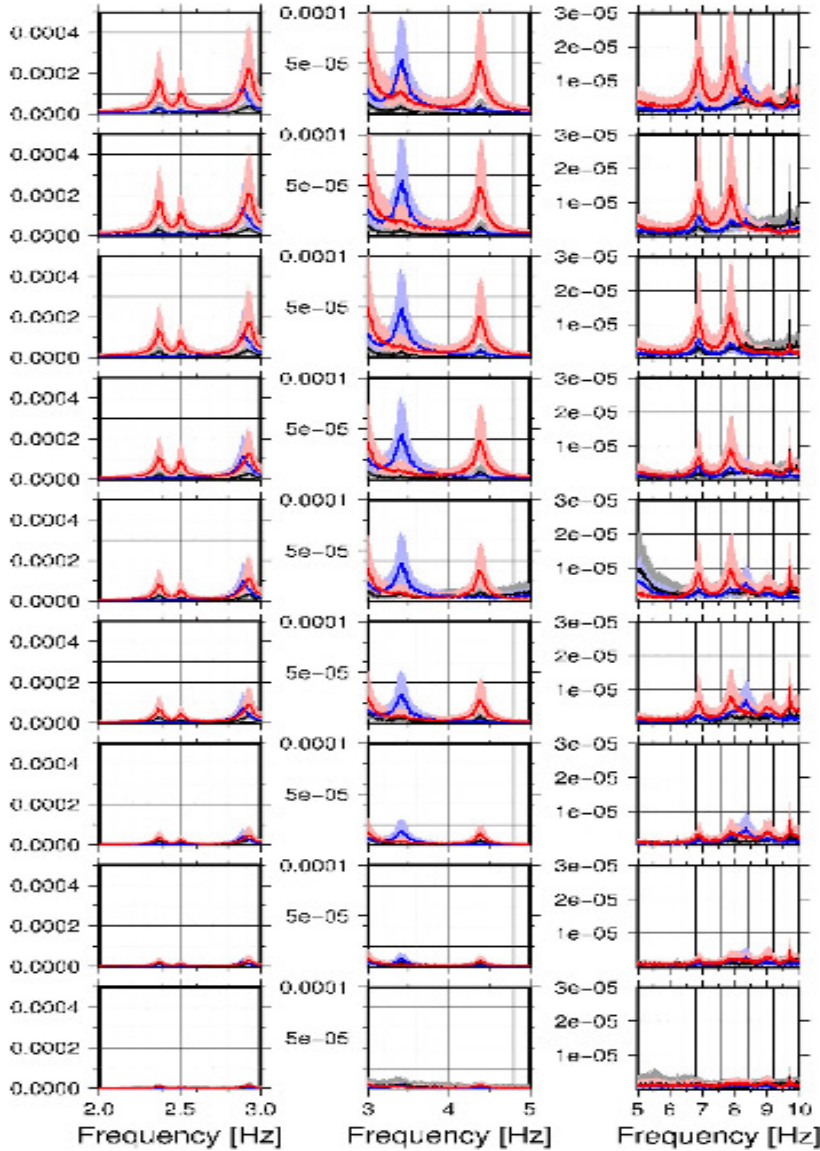


Figure 10.12: Spectra for position D of building 25 at different floors from basement (bottom) to roof (top). The x, y and z components are plotted in blue, red and black respectively. The fundamental mode can be seen on the left (bending in y at 2,37 Hz) very close to a combined mode (2,51 Hz). The first torsional mode (on the right at 2,94 Hz) and flexural mode in x (in the middle at 3,47 Hz) can also be identified. Among the higher modes on the right, two torsional modes can be seen (4,43 Hz and 6,96 Hz).

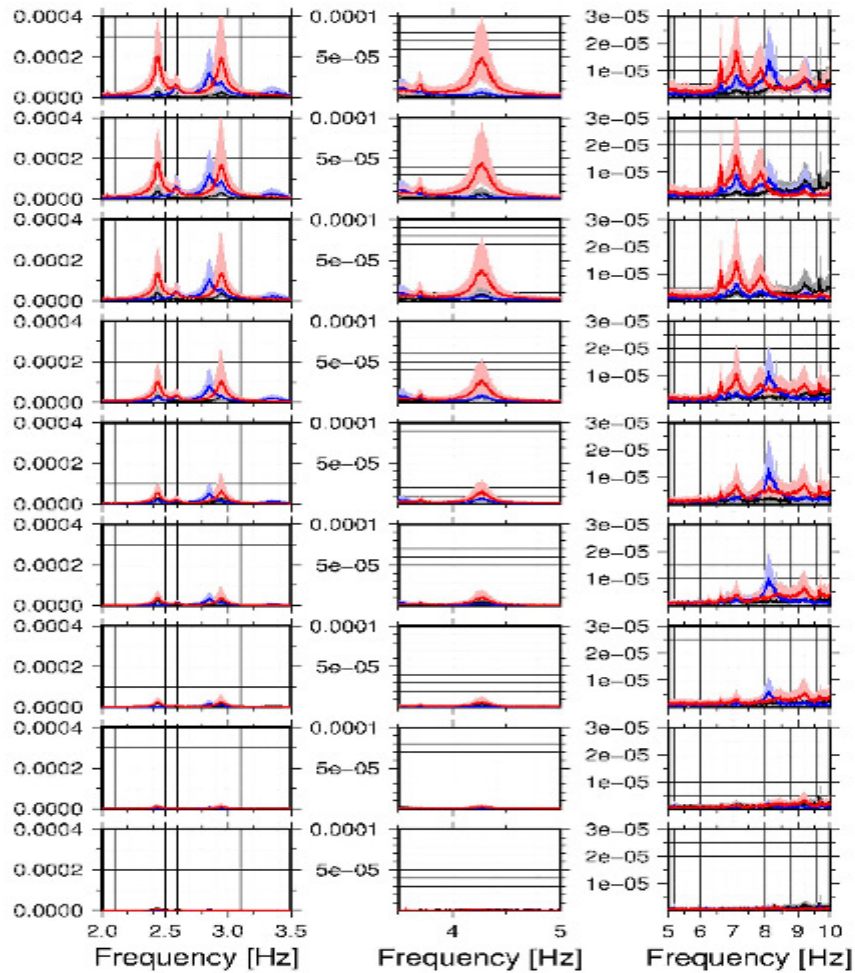


Figure 10.13: Spectra for position A of building 4/1 at different floors from basement (bottom) to roof (top). The x, y and z components are plotted in blue, red and black respectively. On the left, four modes can be seen: bending in y (2,44 Hz), torsion (2,59 Hz), bending in x (2,80 Hz) and torsion (2,93 Hz). In the middle another torsional mode can be identified (4,43 Hz). Among the higher modes on the left a torsional one (6,63 Hz) and flexural one in x (8,12 Hz) can also be seen.

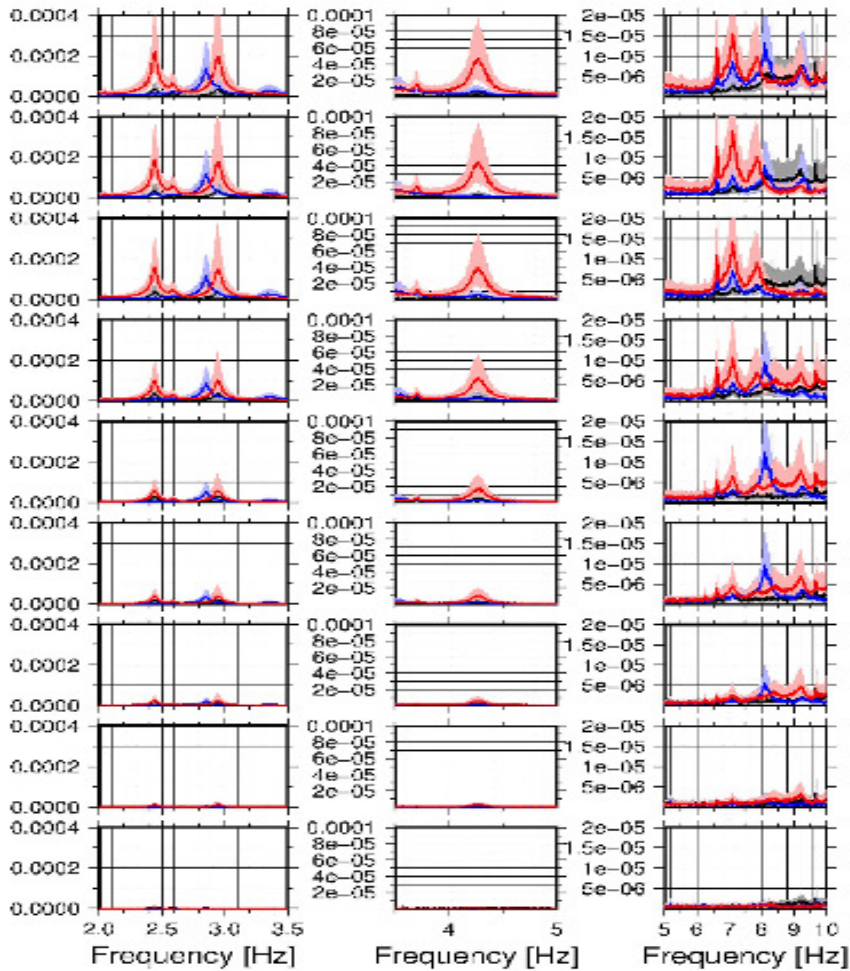


Figure 10.14: Spectra for position B of building 4/1 at different floors from basement (bottom) to roof (top). The x, y and z components are plotted in blue, red and black respectively. On the left, four modes can be seen: bending in y (2,44 Hz), torsion (2,59 Hz), bending in x (2,80 Hz) and torsion (2,93 Hz). In the middle another torsional mode can be identified (4,43 Hz). Among the higher modes on the left a torsional one (6,63 Hz) and flexural one in x (8,12 Hz) can also be seen.

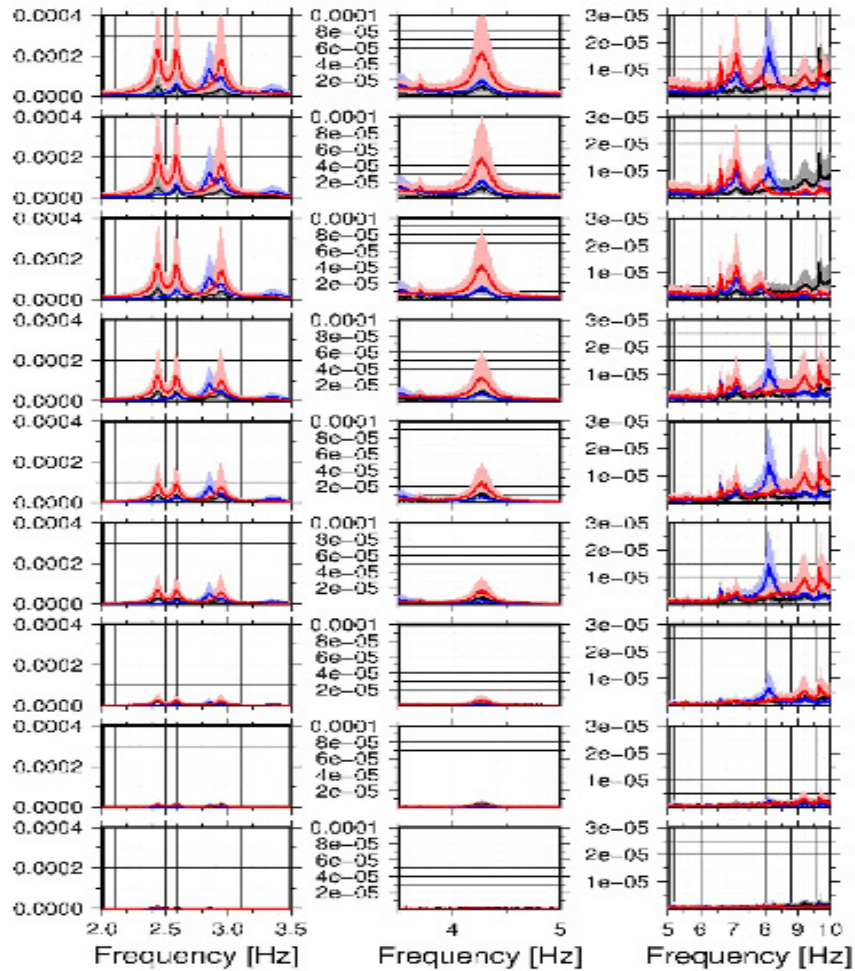


Figure 10.15: Spectra for position C of building 4/1 at different floors from basement (bottom) to roof (top). The x, y and z components are plotted in blue, red and black respectively. On the left, four modes can be seen: bending in y (2,44 Hz), torsion (2,59 Hz), bending in x (2,80 Hz) and torsion (2,93 Hz). In the middle another torsional mode can be identified (4,43 Hz). Among the higher modes on the left a torsional one (6,63 Hz) and flexural one in x (8,12 Hz) can also be seen.

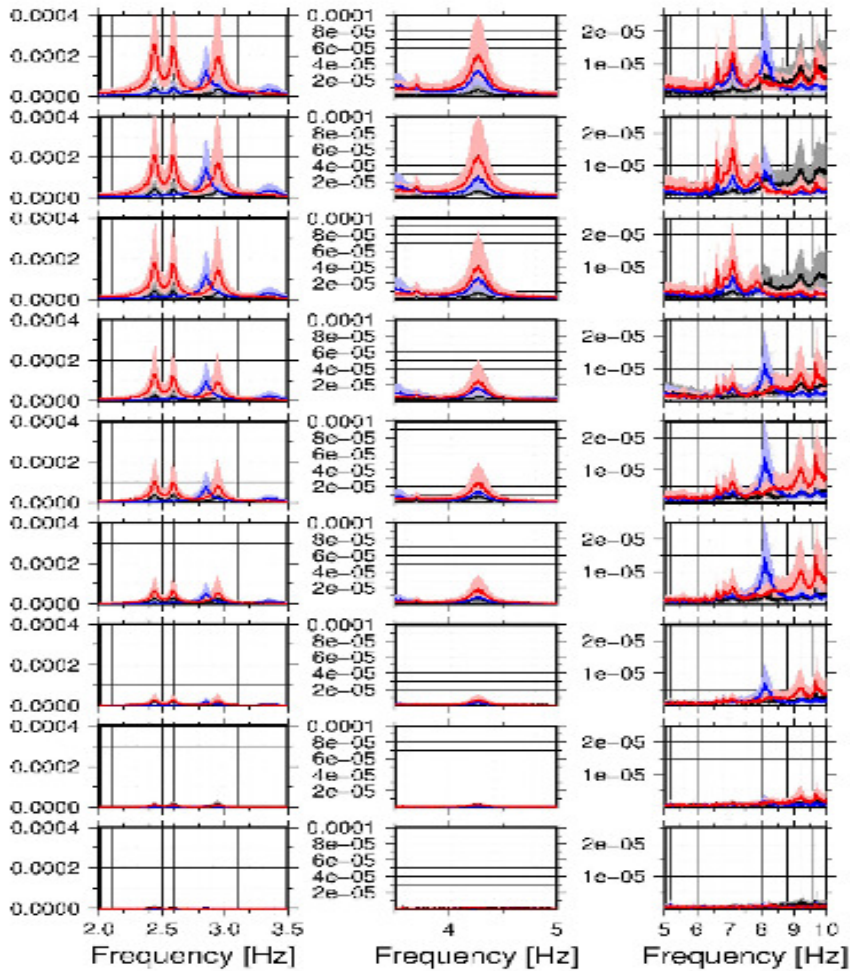


Figure 10.16: Spectra for position D of building 4/1 at different floors from basement (bottom) to roof (top). The x, y and z components are plotted in blue, red and black respectively. On the left, four modes can be seen: bending in y (2,44 Hz), torsion (2,59 Hz), bending in x (2,80 Hz) and torsion (2,93 Hz). In the middle another torsional mode can be identified (4,43 Hz). Among the higher modes on the left a torsional one (6,63 Hz) and flexural one in x (8,12 Hz) can also be seen.

# Acknowledgements

I want to heartily thank Prof. Stefano Parolai for offering me the opportunity to develop this work. It has been a wonderful experience both academically and personally. It would not have been the same without Bojana Petrovic, who strongly supported me, answering any question and revising the work. To her goes the greatest thank you.

On the engineering side, I want to thank Prof. Stefano Silvestri for accepting my thesis proposal and for his precious support, in spite of the distance.

I am also very thankful for the time that Prof. Yuri Petryna took for discussing the building technology with me. It was a honour to partake of his great knowledge.

I then would like to thank all the wonderful *Mitarbeiter* of the Earthquake Risk and Early Warning of the GFZ, who made me feel welcome from the very beginning. In particular, I want to thank Dr. Kevin Fleming for revising my English and for his constant support. The ambient vibrations measurements have been carried out by Dr. Dino Bindi, Sagynbek Orunbaev and Bojana Petrovic; I warmly thank them. I would then like to thank Temirlan Sheraliev, who helped me during the site inspection in Bishkek, and also Dr. Moldobekov, Prof. Lauterjung and again Prof. Parolai for this great opportunity.



It has been a honour to work with all these fantastic people and I feel very grateful.

Finally, I want to spend some words to thank those that have supported me way beyond this work. My boyfriend Fabio, my strongest supporter and my love. My friends and my family. A special thanks to my granny Laura and to my great parents Fernanda and Luigi. They gave my the love and the opportunities that made this all possible.